DOE/ET-53088-303 IFSR#303

Toroidal Studies of Sawtooth Oscillations in Tokamaks

A.Y. Aydemir, J.C. Wiley and *D.W. Ross*
Institute for Fusion Studies
The University of Texas at Austin
Austin, Texas 78712

August 1988

Toroidal Studies of Sawtooth Oscillations in Tokamaks

A. Y. Aydemir, J. C. Wiley[†] *, and D. W. Ross*[‡]
Institute for Fusion Studies
The University of Texas at Austin
Austin, Texas 78712

Abstract

Tokamak sawtooth oscillations are studied with a nonreduced, fully toroidal, resistive MHD (magnetohydrodynamic) model that includes ohmic heating, and parallel and perpendicular thermal conduction. Effects of perpendicular transport in producing different types of sawteeth, varying from simple, periodic oscillations to giant sawteeth with temperature modulations of order unity, and compound sawteeth with multiple relaxations, are demonstrated. Some of the recent experimental observations from large tokamaks, such as the fast crash times and a presumed topological anomaly in the X-ray tomography pictures, thought to be inconsistent with the Kadomtsev reconnection model, are examined and possible explanations are offered.

PACS Numbers: 52.55.Fa, 52.65.+z, 52.35.Py, 52.30.Jb

[†] Fusion Research Center, The University of Texas, Austin, TX 78712.
[‡] Institute for Fusion Studies and the Fusion Research Center.

I. Introduction

Sawtooth oscillations are studied in toroidal geometry using full, nonreduced, resistive magnetohydrodynamic (MHD) equations. Sawtooth oscillations are periodic signals observed in many tokamak diagnostics that are correlated with periodic changes in the core plasma conditions. First observed in the soft X-ray signals[1], now they are a common feature of central electron and ion temperature, and even density[2] measurements.

Kadomtsev heuristically explained these oscillations in terms of the nonlinear evolution of $m = 1$ resistive tearing mode that goes unstable when the central value of the safety factor, q_0, falls below one[3]. This model, subsequently confirmed to a large extent by nonlinear numerical calculations[4], was thought to explain the experimental observations of the time. However, discoveries of such new features as compound sawteeth[5], fast crash times[6], and monster sawteeth[7], coupled with the fact that these oscillations play a crucial role in the confinement in the central region, have contributed to a high level of continuing interest in this ubiquitous feature of tokamak plasmas.

Considerable work has been done recently to explain some of the apparent discrepancies between the Kadomtsev model and observations from present day large tokamaks such as TFTR and JET. Wesson suggested that the ideal internal kink mode, assumed to be stabilized by toroidal effects[8], may play a significant role in fast crashes in JET if the shear-stabilization is eliminated by very flat q-profiles in the center of the tokamak[9]. Since then, both parallel current and pressure driven internal kink modes in low shear systems with $|q - 1| \ll 1$ in the central region have been studied extensively. Hastie et al.[10] examined the stability of a variety of $q-$profiles , both analytically and computationally using a full MHD code, for circular cross-section tokamaks. A similar study by Aydemir[11] found unstable modes both for monotonic, and nonmonotonic profiles with off-axis minima in the $q-$profile, even in the zero$-\beta$ limit. (β is the ratio of the plasma pressure to the magnetic field pressure.) A toroidal analysis by Waelbroeck and Hazeltine[12] appropriate for the weak shear regime, found an unstable mode with no β threshold, in agreement with

previous computational results. Similar studies have examined the stability of non-circular tokamaks, both in the linear[13], and nonlinear regimes[14], again indicating the possible importance of these modes in understanding the sawtooth oscillations in tokamaks.

In parallel with these linear and nonlinear studies of MHD modes, and their role in sawtooth oscillations, there has been an effort to do a more self-consistent study in which the sawtooth oscillations themselves are followed in time. Here, rather than studying the stability of carefully chosen families of equilibria, one follows quasi-periodic oscillations during which a thermal instability self-consistently leads to conditions in which some ideal or resistive MHD mode becomes unstable, and the nonlinear evolution of this mode leads to the crash. The first successfull attempt at producing periodic sawtooth oscillations along these lines was by Denton et al.[15], who qualitatively reproduced some of the experimental observations using a helically symmetric reduced MHD model. However, finite-β has a strong destabilizing influence on these modes[10-14]. In addition, toroidicity plays a crucial role for pressure-driven modes, since cylindrical and toroidal curvature effects tend to cancel for modes resonant at the $q = 1$ surface. Even at zero-β, toroidicity modifies the stability boundary of the internal kink mode [16]. Thus, there is a strong need for a toroidal study of sawtooth oscillations at finite-β.

In this paper, sawtooth oscillations will be examined in the context of nonreduced, toroidal, resistive magnetohydrodynamic equations. We will try to answer some of the recently raised questions regarding crash times, topological differences between experimental observations and the Kadomtsev model, and the fast trigger mechanism. We will also examine various types of sawtooth oscillations produced by different transport models. In the next section, the model equations are presented. Various numerical experiments resulting in different types of sawteeth are discussed in section III. Section IV discusses scaling studies for crash times and sawtooth period. Finally, our results are summarized in Section V.

II. The Model Equations

Numerical studies of sawtooth oscillations are carried out using our toroidal resistive MHD code, CTD, which solves the following set of equations, written in nondimensional form:

$$\frac{\partial \mathbf{u}}{\partial t} + \mathbf{u} \cdot \nabla \mathbf{u} = \mathbf{J} \times \mathbf{B} - \nabla p + \mu \nabla^2 \mathbf{u}, \tag{1}$$

$$\frac{\partial \mathbf{A}}{\partial t} = \mathbf{u} \times \mathbf{B} - \frac{1}{S} \eta \mathbf{J}, \tag{2}$$

$$\frac{\partial p}{\partial t} + \mathbf{u} \cdot \nabla p = -\Gamma p \nabla \cdot \mathbf{u} + \frac{\kappa_{\|}}{B^2} \left(\mathbf{B} \cdot \nabla \right)^2 p + \nabla \cdot \left(\kappa_{\perp} \nabla p \right) + \frac{\Gamma - 1}{S} \eta J^2, \tag{3}$$

$$\mathbf{B} = \nabla \times \mathbf{A}, \text{ and } \mathbf{J} = \nabla \times \mathbf{B}. \tag{4}$$

CTD can also solve the toroidal MHD equations in the incompressible limit, $\nabla \cdot \mathbf{u} = 0$, in which case the equation of state, Eq. 3, is replaced by an appropriate elliptic equation for the pressure field[17]. Above, S is the ratio of the resistive diffusion time to the poloidal Alfvén time, and Γ is the ratio of specific heats. Note that in these equations, density is assumed to be constant (unity). Thus, the pressure field essentially describes the single fluid temperature, and the terms pressure and temperature will be used interchangeably. Resistivity is described by η/S, which is assumed to have a classical dependence on temperature: $\eta \sim p^{-3/2}$. The parallel thermal conductivity coefficient $\kappa_{\|}$, and the kinematic viscosity μ are taken to be constants, both in space and time. The perpendicular thermal conductivity coefficient $\kappa_{\perp}$, and the resistivity η, however, will be allowed to have spatial and temporal variations. The variables have been normalized as follows:

$$t \rightarrow \frac{t}{\tau_{Hp}}, \quad \mathbf{r} \rightarrow \frac{\mathbf{r}}{a},$$

$$\mathbf{B} \rightarrow \frac{\mathbf{B}}{B_{po}}, \quad \mathbf{u} \rightarrow \frac{\mathbf{u}}{u_{Hp}}, \quad p \rightarrow \frac{p}{B_{po}^2/\mu_o},$$

where

$$u_{Hp} = \frac{B_{po}^2}{\sqrt{\rho_o \mu_o}}, \quad \tau_{Hp} = \frac{a}{u_{Hp}}, \quad \tau_R = \frac{\mu_o a^2}{\eta_o}, \quad S = \frac{\tau_R}{\tau_{Hp}}.$$

B_{po} is a characteristic poloidal field strength, and a is the minor radius. The transport coefficients in the pressure equation are normalized as $\kappa_\perp = \tau_{Hp}/\tau_{\kappa_\perp}$, and $\kappa_\parallel = \tau_{Hp}/\tau_{\kappa_\parallel}$, where $\tau_{\kappa_\perp} = a^2/\kappa_{\perp o}$, and $\tau_{\kappa_\parallel} = a^2/\kappa_{\parallel o}$. $\kappa_{\perp o}$, and $\kappa_{\parallel o}$ are the dimensional values of the perpendicular and parallel thermal conductivities, respectively.

In our nonlinear calculations, typical values for the transport coefficients are:

$$S \simeq 10^5 - 10^6, \quad \kappa_\perp \simeq 10^{-4} - 10^{-6}, \quad \mu \simeq 10^{-4} - 10^{-5}, \quad \kappa_\perp \simeq 10^2.$$

For comparison, in large tokamaks like TFTR or JET, the Lundquist number $S \geq 10^8$, and the anomalous value of $\kappa_\perp = (2/3)\chi_e \sim 10^{-7}$, based on a thermal diffusivity of $1m^2/sec$.

In CTD, the nonlinear equations (1-4) are solved using highly efficient semi-implicit techniques[18,19], which make calculations on a transport time-scale possible. In earlier versions of CTD, the nonlinear resistive MHD equations were solved with[17], and without[18] the incompressibility assumption, in cylindrical geometry. The toroidal version of CTD, which solves both the incompressible and the compressible equations, is an outgrowth of these works. It has been used earlier in linear and nonlinear studies of internal kink modes[11].

CTD uses the toroidal coordinate system (r, θ, ζ), where r is the minor radius, and θ, ζ are the poloidal and toroidal angles, respectively. Variables are expanded in double Fourier series of the form

$$\mathbf{u}(r, \theta, \zeta) = \sum_{m,n} \mathbf{u}(r; mn) e^{i(m\theta + n\zeta)},$$

where (m, n) are the (poloidal,toroidal) mode numbers. A finite difference grid is used in the radial direction. In the present work, we use 100-150 grid points, with up to

four toroidal harmonics ($n_{max} = 4$), each with 11 poloidal harmonics. The axisymmetric background ($n = 0$ mode) is described with 6 poloidal harmonics. The details of the numerical techniques used in the present fully toroidal version of CTD will be described elsewhere.

III. Sawtooth Oscillations - Numerical Experiments

All tokamaks exhibit sawtooth oscillations under most operating conditions. Each sawtooth period is divided into two distinct phases. The sawtooth ramp is associated with a thermal instability which preferentially heats up the central region. The heating, however, does not continue indefinitely and is terminated by a sudden drop in the central temperature, the sawtooth crash. The crash, caused by some instability which very rapidly transports heat from the center to the outside, is a relaxation process by which the discharge returns to a state with more stable current and temperature profiles in the center. The ramp phase, which lasts approximately $5 - 10$msec. in small tokamaks like TEXT, and hundreds of milliseconds in large tokamaks like TFTR and JET, is dominated by transport processes. The crash, however, typically occurs in about 100μsec., both in large and small tokamaks, and is assumed to be caused by some ideal or resistive MHD mode.

In order to understand the importance of various transport processes during a sawtooth cycle, here we briefly examine the pressure evolution equation, Eq. 3. Integrating over a volume that includes the central sawtooth region, we get

$$\frac{\partial}{\partial t}\int p dV = \int \frac{(\Gamma - 1)}{S}\eta J^2 dV + \oint \kappa_\perp (\widehat{n}\cdot\nabla p) dS. \tag{5}$$

We have ignored the terms involving the fluid velocity, **u**. The parallel conductivity term drops out if the volume is bounded by a flux surface. In order to have a thermal instability, the ohmic heating term must dominate over the heat flux due to perpendicular transport term. With some obvious approximations, this condition can be put in the form

$$\frac{\eta}{S\kappa_\perp} \gtrsim \widehat{\beta}_p,$$

where $\widehat{\beta_p}$ is a measure of the poloidal β, the ratio of the variation of the kinetic pressure over the volume to the poloidal magnetic field pressure and is given by

$$\widehat{\beta_p} = \frac{2r_s \partial p/\partial r}{B_p^2}.$$

We have assumed that the integrals above extend to r_s, the radius of the $q = 1$ surface. Thus, in our computational discharges, the poloidal beta is approximately determined by the quantity $\eta/S\kappa_\perp$.

During each sawtooth ramp, small changes in the pressure, and current profiles take place, which eventually trigger a crash. These changes can be approximately related to each other as follows. If we assume that the resistivity has a power-law dependence on the pressure (temperature) of the form

$$\frac{\eta}{\eta_o} = \left(\frac{p}{p_o}\right)^{-\nu},$$

then a change in the pressure of magnitude $\delta p/p$ implies $\delta\eta/\eta = -\nu\delta p/p$. If the plasma is in resistive equilibrium at all times during the ramp, $RE_\zeta =$ constant ($R = R_o + r\cos\theta$), this change in resistivity would imply a change in the current density approximately given by $\delta J/J = -\delta\eta/\eta$. However, since the sawtooth period, τ_s, is typically much shorter than the resistive diffusion time $\tau_R = \mu_o r_s^2/\eta_o$, the actual change in the current density will be approximately $\delta J/J = -(\tau_s/\tau_R)(\delta\eta/\eta)$. Then, using $\delta q/q = -\delta J/J$ near the axis, we finally obtain

$$\frac{\delta q}{q} \simeq -\nu \frac{\tau_s}{\tau_R} \frac{\delta p}{p}. \tag{6}$$

An important implication of Eq. 6 is that for $\tau_s/\tau_R \ll 1$, variations in the q-profile during a sawtooth period will be much less than the pressure drop, δp, during the crash. Secondly, sawtooth oscillations would not be possible if we were to decouple the resistivity from the pressure ($\nu \to 0$), since without changes in the toroidal electric field, $E_\zeta = \eta J_\zeta$, no current density enhancement on axis, and thus no change in the $q-$ profile are possible.

The large parallel thermal conductivity ensures that pressure field is an approximate flux function at all times, $p \simeq p(\psi)$, since the time scale associated with $\kappa_\parallel$, $\tau_{\kappa_\parallel} = \left(k_\parallel^2 \kappa_\parallel\right)^{-1}$ is typically faster than any other transport or MHD time-scale. In the absence of parallel thermal conduction, parallel flows and sound waves also tend the equilibriate the pressure along the field lines, but on a much slower time scale.

The perpendicular thermal conductivity, besides its role in defining the β_p for the discharge that was mentioned earlier, is also highly instrumental in producing more complex sawtooth behaviour such as compound, and giant sawteeth.

Throughout this work, the transport coefficients will not have any toroidal variations. In particular, we will have $\eta = \eta(r, \theta, t)$ only, which will prevent certain instabilities, such as the rippling mode, from playing a role in these calculations.

In the remainder of this section, we will discuss various numerical experiments elucidating the effects of these transport processes on sawtooth oscillations.

A. Simple Sawtooth Oscillations

Simple sawtooth oscillations are obtained when only one of the transport coefficients, resistivity η, is coupled to the dynamics. In this section, we will examine in detail sawtooth oscillations produced when we assume $\eta/\eta_o = (p/p_o)^{-3/2}$, but $\kappa_\perp$ =constant. The parameters for this run are: $S = 10^5, \kappa_\parallel = 100, \mu = 10^{-4}$, and a constant thermal conductivity coefficient, $\kappa_\perp = 3.3 \times 10^{-6}$. Volume averaged $\beta = 2.7\%$, and the maximum value of $\epsilon\beta_p$, which occurs just prior to a crash, is $\epsilon\beta_p \simeq 0.1$. Here, the poloidal beta is defined as[8]

$$\beta_p = -\frac{2}{B_\theta^2(r_s)} \int_0^{r_s} \left(\frac{r}{r_s}\right)^2 \frac{\partial p}{\partial r} dr, \tag{7}$$

where r_s is the radius of the $q = 1$ surface. The inverse aspect ratio $\epsilon = a/R_o$ is 1/3 in this work. Note that as defined above, $\beta_p \lesssim 0$ for a large portion of the sawtooth period.

In Fig. 1, signals from a 20-channel "computational soft X-ray array" are shown. Because of the very complex dependence of the soft x-ray emissions on temperature, den-

sity, and impurity concentrations, no attempt is made to calculate the emissions accurately; we plot only the chord-averaged p^2, which emphasizes the hotter regions along the chords. Data produced by CTD is rotated toroidally with a period of $250\tau_{Hp}$ for the purpose of Fig. 1.

Many of the experimentally observed features of soft x-ray signals are also seen in our computational diagnostics. For clarity, only three of the channels are shown in Fig 1c, where we see the signals from the central chord, a chord through the inversion radius, and a chord that clearly passes outside the inversion radius, displaying inverted sawteeth.

Crashes for these relatively high-β runs are characterized by an $m = 1$ pulse that propagates outward all the way to the wall at Alfvénic speeds. It is seen as a spike on soft-x-ray signals during the crash and is observed essentially simultaneously on all the channels (Fig. 1b,c). This non-diffusive pulse represents an adjustment by the whole plasma column to the large amplitude perturbation that occurs in the central region during the crash. Effects of these Alfvénic pulses on diffusive heat-pulse propagation and measurements of thermal diffusivity coefficient need to be examined further.

Below we will use some of the sawteeth of Fig. 1 as examples to discuss the dynamics of the sawtooth ramp and the crash phases, in terms of the $q-$ profile, the field line and pressure profile evolution, and the mode spectra.

The safety factor, q, for the three dimensional magnetic field configurations in our calculations is obtained by following field lines around the torus. Field lines are traced starting with the initial conditions $(r = r(\psi), \theta = 0, \zeta = 0)$, where θ and ζ are the poloidal and toroidal angles, respectively, and ψ is a flux surface label. After a large number of toroidal rotations, $q(\psi)$ is obtained as $q = \zeta/\theta$. In the $q-$profiles shown below, we plot $(q(\psi), < r(\psi) >)$, where $< r(\psi) >$ is the minor radius appropriately averaged over the flux surface.

i) The Sawtooth Ramp

The evolution of the $q-$profile at four different times during a sawtooth ramp

are shown in Fig. 2. Fig. 2a shows the $q-$profile right after a crash. Note that $q \geq 1$ everywhere, with $q = 1$ on axis. In Fig. 2b, ohmic heating, and the accompanying changes in the resistivity and current profiles have led to a $q-$profile with $q \simeq 1$ for a large portion of the plasma column. Note that this $q-$profile presents highly favorable conditions for the growth of a quasi-interchange mode[9-14]. However, as seen in Fig. 2c, q_o continues to fall because of further peaking of the current profile on axis. Fig. 2d shows the profile at the top of the next crash. At this time, $q_o \simeq 0.86 - 0.88$, which is a typical value observed in our calculations for crashes in this parameter regime. The flat reqion with $q = 1$ in Fig. 2d represents a helical flux tube around the original magnetic axis, with a helicity of $m = n = 1$. The algorithm used in obtaining $q(\psi)$ happens to calculate a q for the entire flux tube around its own rotation axis, rather than the rotational transform for the field lines around the magnetic axis of the flux tube. This helical deformation is clearly visible in the magnetic field line plot in the $(r, R_o\zeta)$ plane in Fig. 2e.

The $q-$profile evolution described above is typical for this parameter regime. In summary, it is characterized by three different phases.

i) A stable $q-$profile with $q \geq 1$ everywhere, seen immediately after a crash (Fig. 2a),

ii) A low-shear profile with $q \simeq 1$ in the central region, unstable to a quasi-interchange mode (Fig. 2b), and

iii) A "parabolic", high-shear profile with $q_o \leq 0.9$, unstable to a resistive kink mode (Fig. 2c).

The quasi-interchange mode is characterized by a parabolic eigenfunction[9-14] (Fig. 3a). Because of low-shear, the displacement (or the radial fluid velocity shown in Fig. 3a) does not have to have the step-function profile more characteristic of $m = 1$ modes that is necessary to minimize the stabilizing effects of line-bending when shear is large. However, as q_o continues to drop and shear increases, the quasi- interchange mode is stabilized and is gradually replaced by a resistive kink mode. The eigenfunction for this mode, which exhibits the characteristic rigid displacement of the core, is shown in Fig. 3b.

The linear stability of the slowly evolving plasma column during the ramp is investigated in Fig. 4, where we plot the linear growth rate of the $n = 1$ mode as a function of time for the sawtooth period for $t \in [4.2 - 5.1] \times 10^4 \tau_{Hp}$. The growth rates are obtained by freezing the background and allowing for the evolution of only $n = 1$ modes at various points during the sawtooth ramp. The growth rate γ is defined by

$$\gamma = \frac{1}{2}\frac{1}{E_K}\frac{dE_K}{dt}, \quad \text{where} \quad E_K = \frac{1}{2}\int u^2 dV.$$

Here the volume integral is over the $n = 1$ modes only.

Some of the important features of sawtooth oscillations in this parameter regime can be seen in Fig. 4. First of all, there is a sharp transition from a stable to an unstable state with a growing $n = 1$ mode around $t = 4.60 \times 10^4 \tau_{Hp}$. This "triggger", with a width of approximately $10^3 \tau_{Hp} \sim 100 \mu sec$, was also observed in earlier linear calculations of the ideal quasi-interchange mode[9-11]. However, there it was erroneously associated with the fast triggering of the sawtooth crash itself. As it is seen in Fig. 4, the crash actually occurs at $t \simeq 5.10 \times 10^4 \tau_{Hp}$, approximately $5 \times 10^3 \tau_{Hp}$ after the mode goes unstable; the crash does not immediately follow the onset of the instability, and the sharpness of the sawtooth collapse at $t = 5.1 \times 10^4$ has little to do with the width of the transition layer at $t = 4.6 \times 10^4$. Secondly, comparing the sawtooth period and the length of the unstable period in Fig. 4, we see that there is an unstable mode for over 50% of the sawtooth period. However, the mode amplitude is too small to be seen on any gross diagnostics until the very end of the sawtooth ramp. For instance, since the residual flow left after a crash masks the energy in the growing $n = 1$ mode, the total kinetic energy in the system exhibits a significant growth only at the end of the ramp. Similarly, the displacement of the hot core away from the center, which signifies the beginning of the crash, becomes discernible only around $t = 5.1 \times 10^4$, just before the crash. The evolution of the total kinetic energy and the displacement of the pressure peak for this sawtooth period are shown in Fig. 5. The island width also is a poor diagnostic in this sense since, for $m = 1$, the island width can

be shown to scale as $w \sim B_r$, rather than the usual scaling $w \sim B_r^{1/2}$ observed for $m \geq 2$ modes[20]. Thus, for a given perturbation amplitude B_r, we have $w_{m=1} \ll w_{m=2}$, implying that under most circumstances the $m = 1$ island width remains insignificant until the very end of the ramp, when the mode amplitude increases to $B_r/B_\zeta \sim 10^{-3}$.

The growth rates shown in Fig. 4 were obtained with $S = 1.0 \times 10^5$. Scaling of the growth rate with S for three representative points from Fig. 4 are shown in Fig. 6. The quasi-interchange mode, after a brief ideal period where the growth rate is independent of resistivity (Fig. 6a), also becomes resistive after q_o drops below one (Fig. 6b). For this resistive quasi-interchange mode, the eigenfunction is still parabolic, although the growth rate scales as $\gamma \sim S^{-c}, c \lesssim 1/3$. As q_o drops significantly below one ($q_o < 0.9$) and the requirement for the existence of the quasi-interchange mode, $|1 - q_o| \ll 1$, is violated, the mode becomes a resistive kink mode, with $\gamma \sim S^{-1/3}$(Fig. 6c). Thus, the crash is caused by a resistive kink mode.

ii) The Sawtooth Crash

The computational ECE (electron cyclotron emission) signal for the crash following the sawtooth ramp discussed above is shown in Fig. 7. (As opposed to the "soft-x-ray signals" shown earlier, "ECE signals" are local measurements of the pressure.) The sawtooth crash begins with a helical displacement of the hot core, with a helicity of $m = n = 1$. Various stages of this displacement are seen in Fig. 8. The plots show the evolution of the pressure profile, starting at a point before the crash but with a growing $n = 1$ mode (Fig. 8a). Subsequent figures show the pressure profile at various points during and immediately after the crash. At the toroidal location chosen here ($\zeta = 0$), the displacement is inward along the major radius. As in the low shear calculations[11], the peak is displaced out approximately to the $q = 1$ surface, where it gets deformed into a crescent shape (Figs. 8c,d). However, instead of saturating in an apparent helical equilibrium state in this condition, here the plasma column achieves approximate poloidal symmetry shortly after the displacement is completed (Fig. 8e). The hollow profile of Fig. 8e is then seen to

quickly fill up in Figs. 8f-h because of ohmic heating.

This difference between the nonlinear behavior of the instability seen here and the nonlinear evolution of the quasi-interchange mode studied earlier [11,14] is mainly due to the absence of any significant level of magnetic flux reconnection in the low-shear equilibria with $q_{min} \geq 1$. Without reconnection, flux surfaces get helically distorted, and increasing line bending energy leads to the saturation of the mode. A detailed nonlinear analytic calculation by Waelbroeck has come to similar conclusions[21]. In the present calculations with $q_o \lesssim 0.9$, an $m = 1$ island grows and reconnects the flux within the $q = 1$ surface. Then parallel thermal conduction and perpendicular flows symmetrize the helically shifted pressure profile.

Note that the crescent-shaped pressure profile was previously associated only with the quasi-interchange mode seen in weak-shear profiles[9]. The hot plasma core that forms into a crescent surrounding a cold "bubble" was thought to be an anomaly not explained by the Kadomtsev reconnection process. However, as seen in Fig. 8d, and more clearly in Fig. 9a, in the high-β crashes with $q_o \leq 0.9$ being discussed here, the pressure peak, after being displaced outward to $r \simeq r_s$, again forms into a crescent shape partially surrounding a colder region that was originally part of the $m = 1$ island. Therefore, a cold bubble formation seen on x-ray tomography pictures on JET[6] does not necessarily indicate an active interchange mode, or a $q-$profile with $q \simeq 1$ in the center at all times.

The helical shift in the pressure profile is accompanied by the growth of an $m = 1$ island. The evolution of the island and development and healing of stochastic field lines are shown in Fig. 10. The times for the surface of section plots are indicated by arrows in Fig. 7, where we plot the computational ECE signal from the magnetic axis. Note that there are no visible islands in Fig. 10a, approximately $500\tau_{Hp}$ before the beginning of the crash. Thus, a diagnostic based on the presence of an island would not detect the unstable mode. At the top of the crash, Fig. 10b, and half way down the crash in Fig. 10c, islands of different helicities are present. In addition to the large $m = 1$ island, one can easily

identify $(m,n) = (2,1), (3,2)$, and $(5,2)$ primary island chains. Note also the formation of secondary island chains inside the $q = 1$ surface. In Fig. 10b, $m = 7$, and $m = 9$ chains are clearly visible. These secondary islands, all of which have $n = 1$, are located mainly inside the inner separatrix of the $m = 1$ island. They are caused by the interaction of field lines as they wrap around the $m = 1$ island (with helicity of $(m,n) = (1,1)$) with the axisymmetrix components of the magnetic field with $n = 0$, and $m = 1, 2, 3...M$[22]. As the crash proceeds, interaction of the secondary islands leads to a large band of stochastic region around the island separatrix (Fig. 10d). The development of this stochastic layer, however, does not prevent full reconnection. At the bottom of the crash, after the flux reconnection is complete, stochasticity inside the inversion radius is seen to heal (Fig. 10e).

Stochastic regions develop also outside the inversion radius, around the separatrices of other primary islands such as $(m,n) = (2,1), (3,2)$, and $(4,3)$, as seen in Figs. 9d-g. However, these tend to stay as bands separated by good flux surfaces (KAM surfaces), since the primary islands never become large enough for complete island overlap. After the crash, the stochastic regions gradually shrink and good flux surfaces form (Fig. 10h), as they have done earlier inside the inversion radius.

Figure 11 shows the mode spectra at the top of the crash (Fig. 11a), and in the middle of the crash (Fig. 11b). Although the crash is caused by a mode resonant at the $q = 1$ surface, $(m,n) = (1,1)$ is by no means the dominant mode during this time. The unstable $n = 1$ mode, both during the linear and nonlinear stages of its evolution before the crash, is dominated by the two sidebands, $(m,n) = (0,1)$, and $(2,1)$ as seen in Fig. 11a. Even during the crash, $m = 2$ component tends to have a larger energy than the $m = 1$ mode (Fig. 11b). The dominance by the $m = 2$ mode is in fact responsible for the $m = 2$ structure appearing in the $m = 1$ island in Fig. 10. This effect seems to be due to finite-β, and disappears as β is reduced. For instance, during crashes at $\beta \simeq 0.5\%$ (as opposed to $\beta \simeq 2.7\%$ here), $m = 1$ becomes the dominant mode.

iii) Absence of an Early Saturation Mechanism

An interesting question to ask at this point is why the sawtooth oscillations occur at all. Modifications in the safety factor and pressure profiles occur on the slow transport time scale, whereas the unstable ideal or resistive MHD mode grows on an Alfvénic or hybrid time scale. On the surface, it might seem reasonable to expect the mode to modify the background equilibrium as soon as it goes unstable, thus maintaining the system near marginal stability at all times and preventing any externally discernible relaxation oscillations. The resolution of this apparent paradox lies in the fact that it takes a finite amount of time for the mode to grow to macroscopically significant levels where it can make changes in the current density and pressure profiles. During this period, transport mechanisms can make significant changes in the relevant physical quantities, as discussed below.

At marginal stability, $q \geq 1$ for all r, and $r_s = 0$. (For the puposes of this argument, we will use a simple cylindrical model, although the results are applicable in the toroidal geometry.) Near this marginal stability point, there is a competition between the resistive diffusion of the current towards the center driven by ohmic heating, and the $m = 1$ kink-tearing mode. Ohmic heating tends to increase the current density on axis, thus pushing the rational surface outward. The tearing mode, which goes unstable for $q < 1$ ($r_s > 0$) tries to move r_s back to the axis by reconnecting the flux within the rational surface. The rate for these two processes can be compared as follows: Using a normalization in which $B_\zeta / R_o = 1$, we have for the radius of the $q = 1$ surface,

$$r_s = q_s B_\theta = B_\theta(r_s).$$

Then

$$\frac{dr_s}{dt} = \frac{\partial B_\theta}{\partial r}\frac{dr_s}{dt} + \frac{\partial B_\theta}{\partial t}, \quad \text{or} \quad \frac{dr_s}{dt} = \frac{1}{1 - \frac{\partial B_\theta}{\partial r}}\frac{\partial B_\theta}{\partial t}. \tag{8}$$

Near the marginal point, we have $B_\theta = r + O(r^3)$ (The current density $J \simeq 2$ at the center

in this normalization.) Thus,

$$\left|\frac{dr_s}{dt}\right| \gg \left|\frac{\partial B_\theta}{\partial t}\right|. \tag{9}$$

This equation implies that the rate of change of r_s is much greater than the rate at which the underlying transport process modifies the B_θ (or the current) profile. On the other hand, the tearing mode will restore the system to the marginally stable state with $r_s = 0$ at a rate determined by u_r, the radial fluid velocity with which the flux from the center is carried to the singular surface at $r = r_s$. Note that the restoration of marginal stability requires physical movement of the plasma within the rational surface, whereas the expansion of r_s does not. Obviously, near marginal stability, we will have $|dr_s/dt| \gg |u_r|$. For the tearing mode to catch up with the expansion of the rational surface, first the velocity u_r has to build up to a significant level. (Computationally, the kinetic energy in the $(m,n) = (1,1)$ mode typically grows from $O(10^{-9})$ to $O(10^{-3})$ during the growth period.) Secondly, the expansion rate of r_s has to slow down, which occurs when the $q = 1$ surface reaches regions with large current gradients. Until these two conditions are satisfied, we will have $|dr_s/dt| \gg |u_r|$, resulting in sawtooth crashes with a finite inversion radius and finite amplitude.

During the sawtooth oscillations described in this subsection, the $q-$profile is monotonic, with q_o appreciably below unity before the crash. The crash is driven by a resistive kink mode and is essentially described by the Kadomtsev's reconnection model[3]. In the next subsection, we will consider more complex sawtooth behavior.

B. Complex Sawtooth Oscillations

With only one of the transport coefficients coupled to the dynamics, we obtained simple, periodic sawtooth behavior, as described in the previous subsection. If, in addition to the resistivity η, we let the perpendicular heat conductivity coefficient, $\kappa_\perp$, be strongly influenced by the dynamics, then more complex, seemingly aperiodic sawtooth behavior is

observed. As an example, we will discuss a case where we let

$$\kappa_\perp = \kappa_{\perp o}\left(\frac{p}{p_o}\right)^{-1/2}, \quad \text{and} \quad \eta = \eta_o\left(\frac{p}{p_o}\right)^{-3/2}, \tag{10}$$

with $\kappa_{\perp o} = 5.0 \times 10^{-6}, \eta_o/S = 10^{-5}$. We still have $\kappa_\parallel = 100$, and $\mu = 10^{-4}$. Average toroidal $\beta \simeq 1.8\%$, and the maximum $\epsilon\beta_p \simeq 0.08$, where β_p is again defined by Eq. 7.

Note that we will not try to justify the thermal conductivity model chosen above on any physical grounds but merely note the interesting sawtooth behavior it generates, some features of which are also seen experimentally. As before, only the axisymmetric portion of the pressure field is used in defining the transport coefficients. Thus, $\kappa_\perp = \kappa_\perp(r, \theta, t)$, and $\eta = \eta(r, \theta, t)$ only, with no toroidal variations.

Because of the strong dependence of the transport coefficients on the dynamical state of the system, small changes between successive crashes tend to get amplified during the ramp. Changes in the evolution of the pressure and current density profiles in turn cause changes in the location and the number of $q = 1$ surfaces, thus modifying τ_s, the period, and the crash type.

Sawteeth oscillations in this parameter regime are characterized by giant sawteeth with pressure modulations of order unity, separated by smaller oscillations, some of which in turn exhibit partial relaxation oscillations themselves (Fig. 12). The series of sawteeth seen in Fig. 12 seems to exhibit some degree of periodicity, with each period being comprised of a giant sawtooth, followed by three smaller oscillations, which build up to the giant sawtooth of the next period. The giant sawteeth are approximately located at $t \in [2.1-2.6\times10^4], t \in [3.6 - 4.1 \times 10^4]$, and $t \in [5.0 - 5.6 \times 10^4]$. They are caused by shrinking of the plasma column during the ramp, which increases the radius of the $q = 1$ surface relative to the width of the column. The crash that ensues is rather violent, leaving a large amount of turbulent energy in $n \geq 1$ modes in its wake. It is also accompanied by a high degree of stochasticity in the exterior region. The complex sawtooth behavior that follows is caused by a gradual shrinking of the column again, caused by perpendicular transport, while at

the same time ohmic heating peaks up the center. The relatively large amount of residual energy left in various $n \geq 1$ modes after the crash is partially responsible for the shorter period of the oscillations that follow, since, with a larger initial amplitude, the growth time of the unstable $n = 1$ mode is correspondingly shorter.

Some of these smaller oscillations themselves exhibit quite complex behavior, such as partial relaxations. Below, we will examine one of the compound sawteeth of Fig. 12, shown in greater detail in Fig. 13. The computational ECE signals for this sawtooth period exhibit continuous MHD activity in the periphery, with partial collapses at $t \simeq 3.32 \times 10^4 \tau_{Hp}$, and $t \simeq 3.48 \times 10^4 \tau_{Hp}$, just before the full crash. Partial collapses occur when two $m = 1$ islands that develop at two distinct $q = 1$ surfaces annihilate each other without total reconnection [23] (Figs. 14a-d). Normally, this process would not affect the center of the plasma column. However, in this case, the larger island helically distorts the flux tubes around the original magnetic axis (Fig. 14c), thus slightly perturbing the center.

The locally flattened $q-$profile after this partial collapse continues to evolve under the influence of ohmic heating and other transport processes. The sawtooth ramp is terminated when total reconnection is made energetically possible by a lower q_o. The crash involves again two $m = 1$ islands (Fig. 14e-h). The outer island first annihilates the inner island (Fig. 14f), and then grows to completely reconnect the remaining flux within the outer resonance surface (Figs. 14g-h).

The double $m = 1$ island structure is caused by an off-axis minimum in the $q-$profile produced by surface currents[23]. These currents can be generated by two related mechanisms: a) A "hollow" pressure profile will draw current into an annular channel of higher conductivity, or b) a pressure profile that peaks while shrinking in minor radius under the simultaneous influence of ohmic heating and perpendicular transport will channel current inward from the cooler periphery, creating an annulus with a higher current density than in the center. The pressure profile in our calculations, although hollow immediately after a crash, tends to become monotonic rather quickly. Thus, it is usually the second

mechanism that generates the surface currents observed when $\kappa_\perp = \kappa_\perp(p)$.

In order to clearly illustrate the significance of perpendicular transport on the evolution of the current profile during the ramp and the type of sawtooth observed, we have performed one dimensional transport simulations using the simple coupled system for the pressure and the current density:

$$\frac{\partial p}{\partial t} = (\Gamma - 1)\,\eta J^2 + \frac{1}{r}\frac{\partial}{\partial r} r \kappa_\perp \frac{\partial p}{\partial r}, \tag{11}$$

$$\frac{\partial J}{\partial t} = \frac{1}{r}\frac{\partial}{\partial r} r \frac{\partial \eta J}{\partial r}, \tag{12}$$

with

$$\eta = \eta_o\,(p/p_o)^{-3/2}, \quad \kappa_\perp = \kappa_{\perp o}\,(p/p_o)^{-\lambda}. \tag{13}$$

The initial conditions and the subsequent evolution of the pressure and the current profiles for different values of λ are shown in Fig. 15. For $\kappa_\perp = \kappa_{\perp o}$ = constant ($\lambda = 0$), the pressure field evolves into a nearly parabolic profile, with no surface currents. For increasing values of λ, the profile contracts in minor radius with subsequent generation of surface currents. Note that the current density (and the $q-$profile) becomes non-monotonic, although the pressure field remains monotonic. This process is similar to our observations in 3D calculations (with $\lambda = 1/2$ in Eq. 13) where the $q-$profile develops an off-axis minimum although the pressure profile maintains $\partial p/\partial r \leq 0$ for all r. In 1D calculations, when followed further in time, the off-axis maximum in the current density seen for $\lambda > 0$ moves inward to the axis. However, in a self-consistent calculation, the current density profile shown in Fig. 15 for $\lambda = 1/2$ would be unstable to a resistive kink and lead to a crash.

IV. Scaling Studies

Even with the highly efficient techniques employed in CTD, it is still not feasible to carry out our sawtooth studies with realistic parameters. For large tokamaks of today, the Lundquist number S exceeds 10^8, whereas, mainly for reasons of economy, computational studies are carried out typically with $S \simeq 10^5 - 10^6$. Therefore, to be able to extrapolate our results to realistic tokamak regimes, we need to carry out a series of scaling studies, with various values of the relevant transport coefficients. However, such a study has to be done without upsetting the dynamic equilibrium among various transport mechanisms, the existence of which is implied by the presence of periodic or quasiperiodic sawtooth oscillations. As discussed at the beginning of Section III, there is a balance, in a time-averaged sense, between the ohmic heating rate determined by resistivity η, and the heat flux to the wall determined by the perpendicular heat transport coefficient, $\kappa_\perp$. Thus, in a scaling study involving resistivity, these two coefficients need to be changed accordingly.

We have carried out a series of calculations where we let

$$S \to \alpha S, \quad \text{and} \quad \kappa_\perp \to \kappa_\perp/\alpha, \tag{14}$$

thus maintaining the aforementioned balance, with different values of the parameter α in order to determine how the sawtooth period and the crash time scale with S. A constant-$\kappa_\perp$ model (simple sawteeth) is used here.

Scaling of the sawtooth period, τ_s, with S is shown in Fig. 16. For $S \leq 1.6 \times 10^6$, the scaling is approximately linear, $\tau_s \sim S$. (The actual slope of the solid line, representing a best fit to the data, is 0.89.) This result can be understood easily by examining a subset of the nonlinear equations, Eqs. (1-4), relevant to the sawtooth ramp:

$$\frac{\partial \mathbf{A}}{\partial t} = -\frac{1}{S}\eta \mathbf{J}, \tag{15}$$

$$\frac{\partial p}{\partial t} = \frac{\kappa_\parallel}{B^2}\left(\mathbf{B}\cdot\nabla\right)^2 p + \nabla\cdot\left(\kappa_\perp \nabla p\right) + \frac{\Gamma - 1}{S}\eta J^2, \tag{16}$$

Note that we have dropped terms involving the fluid velocity, since during the ramp, the transport dominates over the convective terms. By simple inspection we see that the Eqs. (15,16) are invariant under the transformation

$$S \rightarrow \alpha S,$$

$$\kappa_\perp \rightarrow \kappa_\perp/\alpha,$$

$$\kappa_\parallel \rightarrow \kappa_\parallel/\alpha, \tag{17}$$

$$t \rightarrow \alpha t.$$

Thus, this transformation merely changes the time scale of the sawtooth ramp, and the result of our study, $\tau_s \sim S$, is quite expected.

During the scaling study of Fig. 16, the parallel transport and viscosity coefficients were not varied. The effect of $\kappa_\parallel$ on τ_s seems to be negligible for sufficiently large values of $\kappa_\parallel$. Keeping viscosity constant is consistent with dropping the convective terms above.

Scaling of the crash time, τ_c, with S is of vital importance, since the unusually fast crash times observed in large tokamaks[7,9] was the impetus behind much of the recent work in this area. Scaling of τ_c in our calculations with S is shown in Fig. 17. Data from two different sets of scaling studies is presented. In Fig. 17a, the viscosity coefficient μ is held fixed, while S is varied. In Fig. 17b, both the resistivity and viscosity are varied while holding the quantity $S\mu$ constant. The definitions of the crash time τ_c also differ slightly for the two cases. In Fig. 17a, τ_c is defined to be the time interval between the maximum and the minimum of the computational soft x-ray signal through the central chord. In Fig. 17b, τ_c is taken to be the interval from $p_{max} - 0.1\delta p$ to $p_{min} + 0.1\delta p$, where $\delta p = p_{max} - p_{min}$. The solid lines represent best fits to the data. In Fig. 17a, the slope is 0.55, whereas the line in Fig. 17b has a slope of 0.45. Thus, the crash time is seen to scale approximately as $\tau_c \sim S^{1/2}$, in agreement with Kadomtsev's heuristic estimate[3]. Extrapolating to $S = 10^8$ from the data presented in Fig. 17, we obtain $\tau_c \sim 2 - 6 \times 10^3 \tau_{Hp}$. The poloidal Alfvén

time, for tokamaks operating today is $\sim 1-2\times 10^{-7}$sec. (For JET, $1\tau_{Hp}\sim 0.2\mu$sec. for $B_T=3T, n=2\times 10^{19}m^{-3}$.) Thus, we obtain crash times of $500-1000\mu$sec. This result is slower than the 100μsec. crash times observed on JET[7] and other tokamaks. However, it is within an order of magnitude of experimental observations and points to the possibility of explaining the fast crashes in terms of the Kadomtsev reconnection process[3] driven by an $m=1$ kink-tearing mode.

V. Discussion and Summary

We have studied tokamak sawtooth oscillations using a nonreduced, toroidal, full MHD model. One of our goals in this study was to understand some of the apparent discrepancies between recent observations and Kadomtsev's model of the sawtooth collapse[3]. Two of the most significant anomalies are assumed to be the fast crash times, on the order of 100μsec., reported by JET and TFTR[6], and a discrepancy in the topology of crashes (cold bubble formation) reported by JET[7]. We will address these points separately:

i) *The Fast Crash Times*

In order to explain the crash times of $\sim 100\mu$sec., an ideal, pressure driven (quasi-interchange) mode was proposed as the crash mechanism[9]. Linear and nonlinear studies[11,14] of these modes in weak-shear equilibria have indicated that they may in fact be responsible for some of the recent experimental observations from large tokamaks. However, in our self-consistent studies where the sawtooth oscillations are followed on a transport time scale, we find the role played by the ideal quasi-interchange mode to be insignificant. During the sawtooth ramp, we observe a brief period during which the ideal mode is active. However, the weak-shear $q-$profile with $q\gtrsim 1$ in the central region is modified by ohmic heating such that, first we see $q\lesssim 1$ in the center, which converts the ideal mode into a resistive interchange, with a similar eigenfunction but with a growth rate that is now a function of the resistivity. Then, as q_o continues to drop below one, the weak-shear conditions are lost, with $q_o\lesssim 0.9$, and the mode becomes a resistive kink. The

sawtooth crash is thus caused not by an ideal mode, but by a resistive kink, the growth rate of which is seen to scale as $\gamma \sim S^{-1/3}$.

These results were obtained with $S \lesssim 2 \times 10^6$. For large tokamaks, $S \geq 10^8$. Thus, at realistic values of S, the disparity between the transport time scale, the time scale on which the $q-$profile changes, and the growth time of the ideal mode is enhanced. Thus, one might expect an ideal quasi-interchange-driven crash under more realistic conditions where the mode has sufficient time to grow. However, without significant flux reconnection, that scenario seems unlikely, as earlier studies have found this mode to saturate in a helical equilibrium[11,14]. Although the displacement of the core away from the center during this helical shift may be interpreted as a sawtooth crash, eventual poloidal symmetry observed experimentally after the crash was never seen in those studies.

Our scaling studies with the resistive kink mode, however, yield promising, if not conclusive results. As discussed in the last section, we obtain crash times of $500-1000\mu$sec. for $S = 10^8$. Although slower than experimental observations, this result does not rule out the Kadomtsev reconnection process as the cause of the fast crashes. Our studies are continuing in this area, and further exploration with different transport models may indeed give crash times of $\lesssim 100\mu$sec.

ii) *The Bubble Formation*

X-ray tomography studies from JET[7] indicate a cold "bubble" formation during the crash that is partially surrounded by a hot crescent-shaped region. This was contrasted with the cold, crescent-shaped island of the Kadomtsev model, and in order to explain this presumed anomaly, again the quasi- interchange mode was invoked[9]. Indeed, nonlinear studies[11,14] did find close agreement between the nonlinear phase of this mode and the bubble observations from JET. However, as we show in Section III, the hot crescent is observed even with resistive kink modes (Fig. 9). This topological feature is found to be a finite-β effect that results from the hot core being displaced violently towards the $q = 1$ surface, where it gets deformed into the observed semi-circular region partially enclosing

a cold "bubble". Thus, we do not see an inconsistency between this feature of the JET crashes and the Kadomtsev model.

Some of the other points discussed in this article are as follows:

iii) *The Fast Trigger Problem*

An important issue in the recent literature has been the sudden transition from the sawtooth ramp to the crash. This fast trigger has been previously interpreted to imply that the mode causing the crash has to be "turned on" in a time shorter than the crash time τ_c itself. This point is also contradicted by our studies. We see an unstable mode growing for a substantial portion of the sawtooth period (Fig. 4). The crash represents the final stages of the nonlinear evolution of the mode, the resistive kink in our case, and occurs quite a long time ($\gtrsim 10\tau_c$) after the mode goes unstable. During most of the period when the mode is growing, it is not detected by gross diagnostics such as island width, the total kinetic energy, or the displacement of the temperature peak. In fact, observations of these quantities would erroneously lead one to believe that the crash is caused by a mode triggered only a brief period ($\sim \tau_c$) before the crash (Fig. 5). The fast trigger is a result of the hot core being displaced rapidly by a mode that has gone through many e-folding periods, not by a mode that suddenly goes unstable. Admittedly, this argument does not quantitatively explain the trigger-problem. However, it indicates that correllating the trigger with a mode that is switched on in a period of $\sim \tau_c$ is incorrect.

iv) *Transport Effects on Sawteeth*

We have also examined the effects of transport on the type of sawtooth oscillations using simple models for the perpendicular heat transport coefficient, $\kappa_\perp$. With a constant $\kappa_\perp$, we obtained simple, periodic sawteeth. When the time-evolution of $\kappa_\perp$ was coupled to the dynamics by letting $\kappa_\perp \sim p^{-1/2}$, we observed more complex sawteeth behavior involving giant sawteeth with temperature modulations of order unity, interspersed with smaller oscillations, some of which exhibited multiple partial relaxations. We observed that the off-axis minima in the $q-$ profile (cause of compound sawteeth) was not necessarily

associated with a hollow temperature profile, but that it can result from a contraction of the plasma column due to large heat flux to the wall when $\kappa_\perp \sim p^{-1/2}$ (thus large near the wall).

v) *Ballistic Heat Pulse*

For the plasma β considered here (toroidal $\beta \simeq 2\%, \epsilon\beta_p \simeq 0.1$), the crash is followed by a compressional wave that propagates out to the wall; the crash is felt almost simultaneously at all radii, as seen in the computational soft x-ray signals of Fig. 1. In this β range, the crash represents a significant perturbation to the plasma column. Flattening of the pressure and current density profiles in the center modifies the global MHD equilibrium, and the column readjusts itself to establish a new equilibrium. The pulse that propagates outward from the inversion radius represents this adjustment. The effects of this ballistic wave on the diffusive portion of the heat pulse and thermal diffusivity, χ_{Hp}, measurements need to be investigated further.

vi) *Crash-Induced Stochasticity*

A large degree of crash-induced stochasticity was observed for short periods after each crash for the β values considered here ($\epsilon\beta_p \sim 0.1$). The effects of this stochastic period on heat transport can be significant and needs to be investigated carefully.

The crashes studied here involved total reconnection of the flux within the $q = 1$ surface, which necessarily raises q_o to unity at the end of the crash. Sawtooth oscillations with low-q profiles[24,25], $q_o \lesssim 0.7$, which presumably does not involve total reconnection, are not addressed by this article.

Acknowledgements

The authors are grateful for stimulating discussions with various members of the IFS/FRC Sawtooth Study Group. In particular, we would like to acknowledge contributions from D. Brower, J. Chen, R. Denton, M. Foster, K. Gentle, R.D. Hazeltine, S.K. Kim, S. McCool, W. Miner, P. Phillips, B. Smith, P. Valanju, F. Waelbroeck, and A. Ware. Separate discussions with John Wesson on various aspects of this work are also acknowledged.

This work was supported by the U.S. Department of Energy contract #DE-FG05-80ET-53088.

References

1. S. von Goeler, W. Stodiek, and N. Sauthoff, Phys. Rev. Lett. **33**, 1201 (1974).
2. S. K. Kim, D. L. Bower, W. A. Peebles, and N. C. Luhmann, Jr., Phys. Rev. Lett. **60**, 577 (1988).
3. B. B. Kadomtsev, Fiz. Plazmy **1**, 710 (1975) [Sov. J. Plasma Physics **1**, 389 (1975)].
4. B. V. Waddell, M. N. Rosenbluth, D. A. Monticello, and R. B. White, Nuclear Fusion,**16**, 3 (1976).
5. J. Snipes, T. P. Kochanski, S. B. Kim, B. Richards, W. L. Rowan, and P. Phillips, Bull. Am. Phys. Soc. **28**, 1034 (1983), W. Pfeiffer, Nucl. Fusion **25**, 673 (1985).
6. D. J. Campbell et al. in Proceedings of the Twelfth European Conference on Controlled Fusion and Plasma Physics, Budapest, Hungary (1985), Vol. 1 , p. 130, K. McGuire et al., ibid. Vol. 1, p. 134.
7. A. W. Edwards et al., Phys. Rev. Lett. **57**, 210 (1986).
8. M. N. Bussac, R. Pellat, D. Edery, and J. L. Soule, Phys. Rev. Lett. **35**, 1638 (1975).
9. J. A. Wesson, Plasma Phys. Controlled Fusion **28**, 243 (1986).
10. R. J. Hastie, T. C. Hender, B. A. Carreras, L. A. Charlton, J. A. Holmes, Phys. Fluids **30**, 1756 (1987).
11. A. Y. Aydemir, Phys. Rev. Lett. **59**, 649 (1987).
12. F. L. Waelbroeck, R. D. Hazeltine, Phys. Fluids **31**, 1217 (1988).
13. J. J. Ramos, Phys. Rev. Lett. **60**, 523 (1988).
14. J. A. Holmes, B. A. Carreras, L. A. Charlton, V. E. Lynch, R. J. Hastie, T. C. Hender, Phys. Fluids **31**, 1202 (1988).
15. R. E. Denton, J. F. Drake, R. G. Kleva, and D. A. Boyd, Phys. Rev. Lett. **56**, 2477 (1986).

16 A. Ware, Phys. Rev. Lett. **26**, 652 (1971).

17. A. Y. Aydemir, and D. C. Barnes, J. Comp. Phys. **53**, 100 (1984).

18. A. Y. Aydemir, and D. C. Barnes, J. Comp. Phys. **59**, 108 (1985).

19. D. S. Harned, and D. D. Schnack, J. Comp. Phys. **65**, 57 (1986).

20. R. D. Hazeltine, J. D. Meiss, and P. J. Morrison, Phys. Fluids **29**, 1933 (1986).

21. F. L. Waelbroeck, Institute for Fusion Studies Report, IFSR #331, July, 1988.

22. A. J. Lichtenberg, Nucl. Fusion **24**, 1277 (1984).

23. V. V. Parail and G. V. Pereverzev, Fiz. Plazmy **6**, 28 (1980) [Sov. J. Plasma Physics **6**, 14 (1980)].

24. H. Soltwisch, W. Stodiek, J. Manickam, J. Schlüter, in Plasma Physics and Controlled Nuclear Fusion Research 1986 (Proc. of the 10^{th} Int. Conf. Kyoto, Japan 1986), Vol. I IAEA, Vienna (1987) 263.

25. W.P. West, D.M. Thomas, and J.S. deGrassie, Phys. Rev. Let. **58**, 2758 (1987).

Figure Captions

1. a) Computational soft x-ray array used in the calculations. b) Output from the array for the case with constant $\kappa_\perp$. (Output from all twenty channels are shown.) c) For clarity only three channels are shown. The top figure is from the central channel, the middle one through the inversion radius, and the bottom one from a channel outside the inversion radius.
2. The time evolution of the q–profile for constant $\kappa_\perp$. a) $t = 4.252 \times 10^4$, b) $t = 4.504 \times 10^4$, c) $t = 5.006 \times 10^4$, d) $t = 5.089 \times 10^4$. Times are in units of the poloidal Alvén time τ_{Hp}. e) Field lines in the toroidal $(r, R_o\zeta)$ plane showing the $m = 1$ island and the helical deformation of the flux surfaces around the magnetic axis. Negative values of r corresponds to $\theta = \pi$ plane.
3. Radial fluid velocity, u_r, as a function of minor radius. a) Quasi-interchange mode at $t = 4.570 \times 10^4$, b) the resistive kink mode at $t = 5.006 \times 10^4$. Note that during this particular crash, the velocity is negative. (We are accustomed to seeing a positive displacement, ξ, for the eigenfunction.)
4. The linear growth rate of the $n = 1$ mode during a simple sawtooth period. Soft X-ray signal from the central chord for this period is also shown (dashed-line).
5. a) The evolution of the total kinetic energy in the system during the sawtooth period of Fig. 4. b) The displacement of the pressure peak during the crash. Only the portions with $d\xi/dt > 0$ are meaningful.
6. Scaling of the growth rate, γ with S for three points in Fig. 4. a) $t = 4.598 \times 10^4$, ideal quasi-interchange mode with $\gamma \sim S^0$ scaling, b) $t = 4.626 \times 10^4$, c) $t = 5.058 \times 10^4$, resistive kink with $\gamma \sim S^{-1/3}$ scaling.
7. The computational ECE (electron cyclotron emission) signal from the magnetic axis for the crash at $t = 5.1 \times 10^4 \tau_{Hp}$, plotted without the effects of plasma rotation. Unlike the soft x-ray signals shown in Fig. 1, the ECE signals are local measurements of the pressure (temperature). Times for the pressure and field line

plots shown in Figs. 8 and 10 are indicated by arrows here.

8. The time evolution of the pressure field. The perspective plots are from an angle of $\theta = -\pi/3$. The displacement is inward along the major radius.
9. Pressure contours towards the end of the crash discussed in Sec. III.b, showing a crescent-shaped high pressure(temperature) region that was previously associated only with quasi-interchange modes. Figure b) shows the pressure along the midplane.
10. The field line plots during a crash (Simple Sawteeth). Note the development and healing of stochastics regions, first inside the separatrix of the $m = 1$ island, then in the exterior.
11. The mode spectra showing the magnetic energy in various modes. a) For $n = 1, 2$ at the top of the crash of Fig. 7, b) during the crash for $n = (1 - 4)$. Note the dominance of the sidebands, $(m, n) = (0, 1)$ and $(2, 1)$ in a).
12. Computational ECE signals for the case with $\kappa_\perp = \kappa_{\perp o}(p/p_o)^{-1/2}$. Numbers on the right hand side indicate the minor radius of the source of the signal. The top figure is for the magnetic axis. The middle and bottom figures are from points progresively further out in major radius.
13. ECE signals from three radial points during a compound sawtooth (Section III.b).
14. Field line plots for the compound sawtooth of Fig. 13. a) $t = 3.201 \times 10^4$, b) $t = 3.253 \times 10^4$, c) $t = 3.322 \times 10^4$, d) $t = 3.394 \times 10^4$, e) $t = 3.511 \times 10^4$, f) $t = 3.530 \times 10^4$, g) $t = 3.537 \times 10^4$, h) $t = 3.579 \times 10^4$.
15. Evolution of pressure and current density profiles from a one dimensional calculation, showing the effects of variations in the perpendicular thermal conductivity coefficient, assumed to have the form $\kappa_\perp = \kappa_{\perp o}\,(p/p_o)^{-\lambda}$. The numbers indicate values of λ. a) The initial conditions, approximately similar to the profiles seen after a crash in three dimensional calculations. b) The profiles at $t = 3.0 \times 10^3$, for $S = 10^5$ and $\kappa_{\perp o} = 1.0 \times 10^{-5}$.

16. Sawtooth period as a function of the Lundquist number S.

17. Sawtooth crash time as a function of S. a) Sawtooth crash time is defined as the period between the maximum and the minimum of the central soft x-ray signal. During this scaling study, the viscosity coefficient, μ, was held fixed. b) Here τ_c was defined to be the central 90% of the period defined in (a), and $S\mu$ was held fixed.

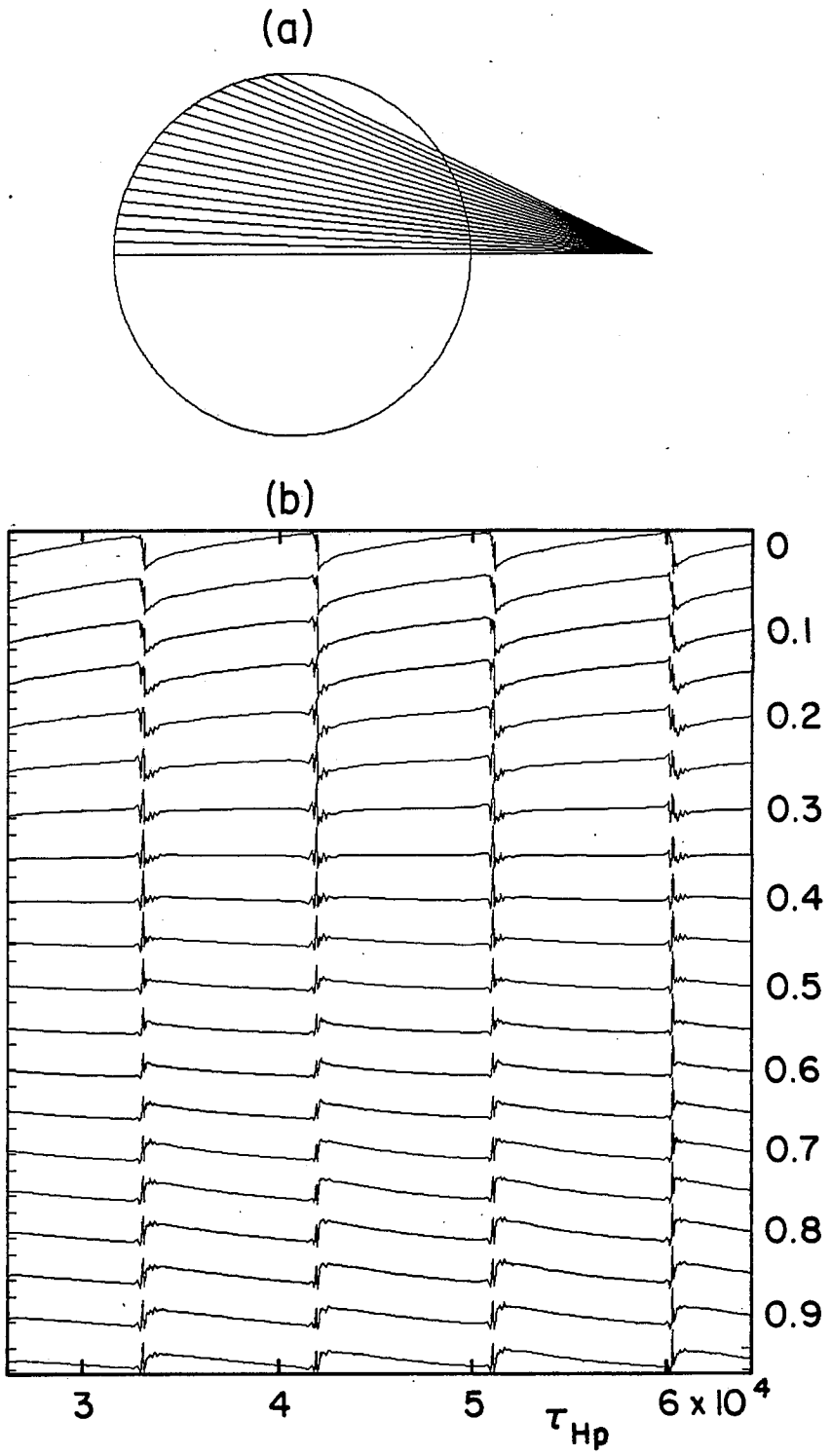

Fig. 1(a-b)

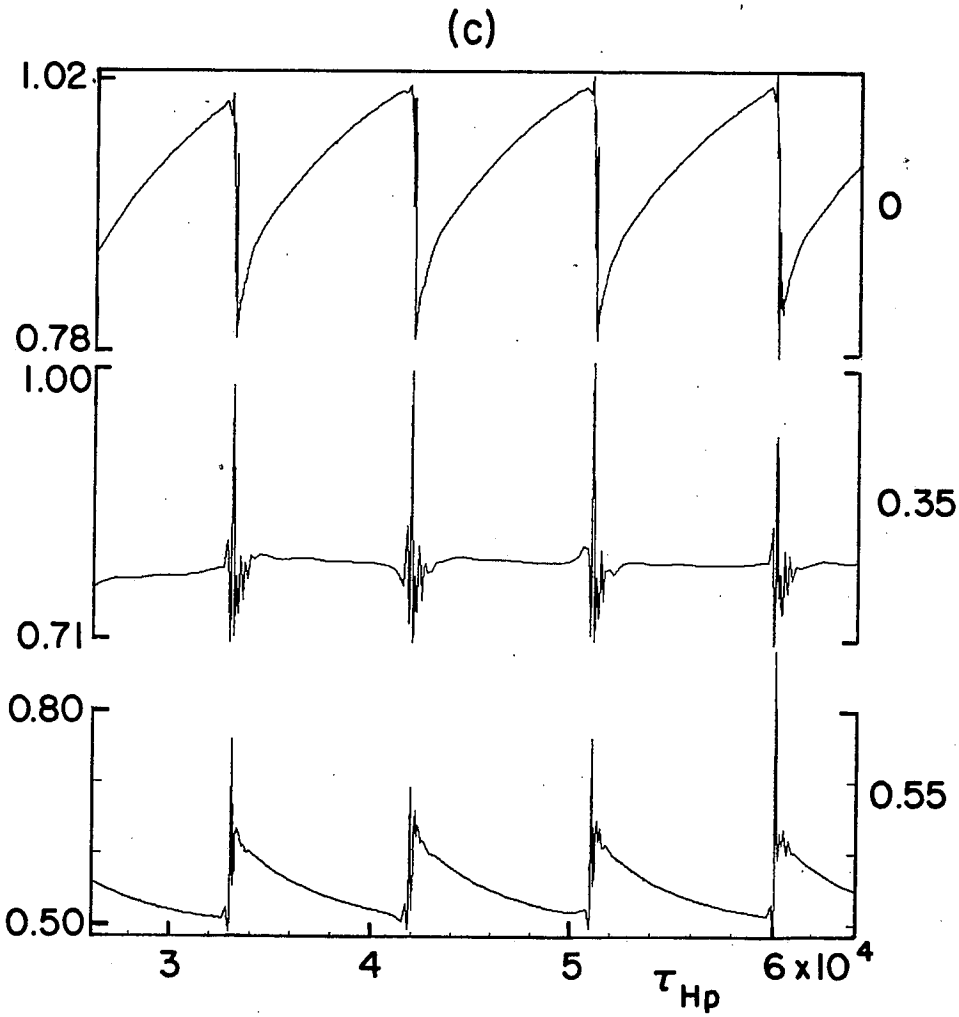

Fig. 1(c)

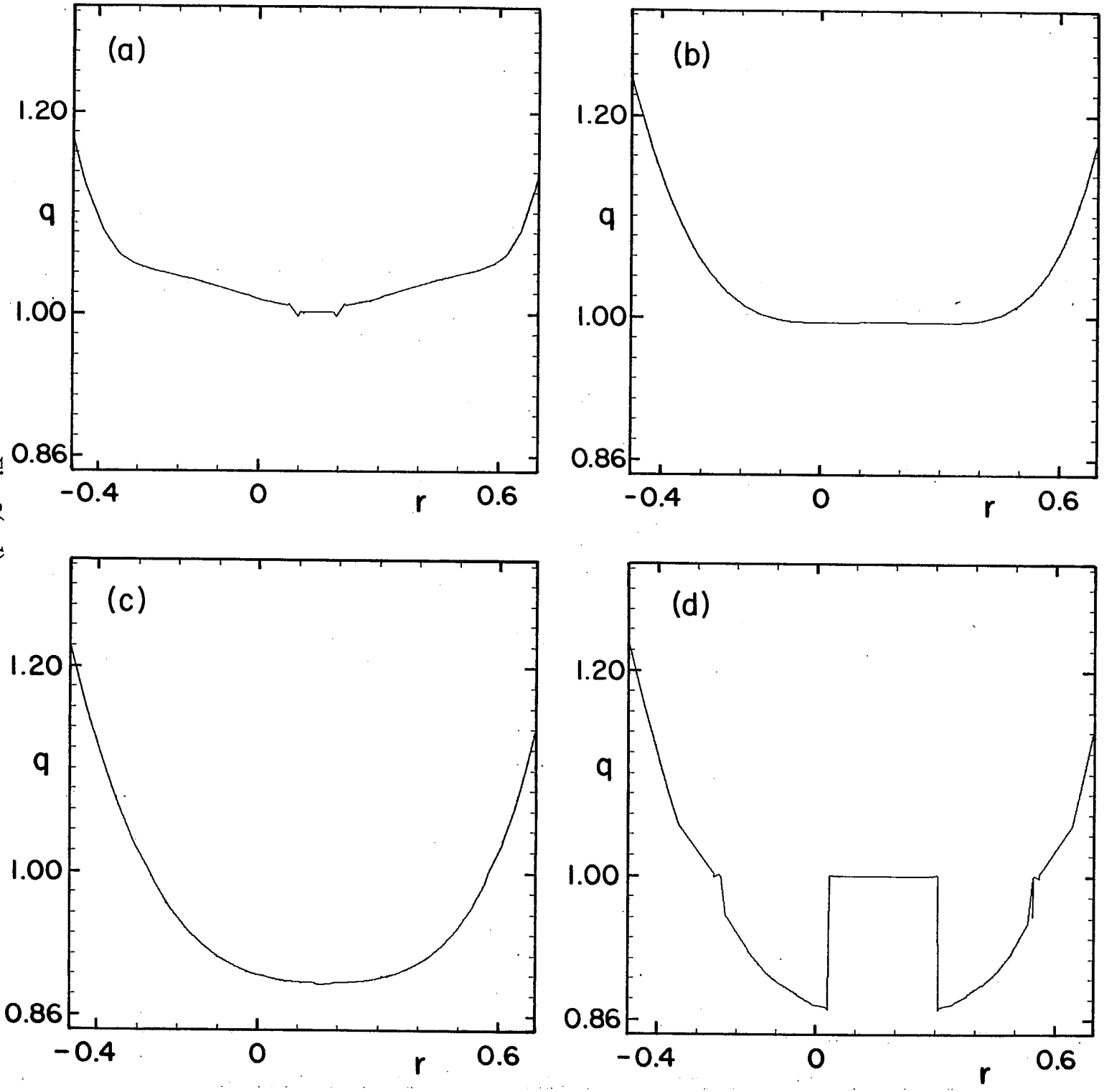

Fig. 2(a-d)

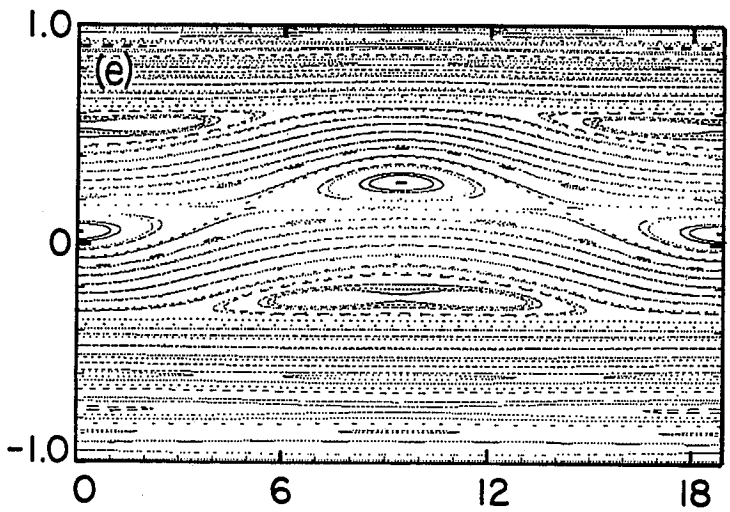

Fig. 2(e)

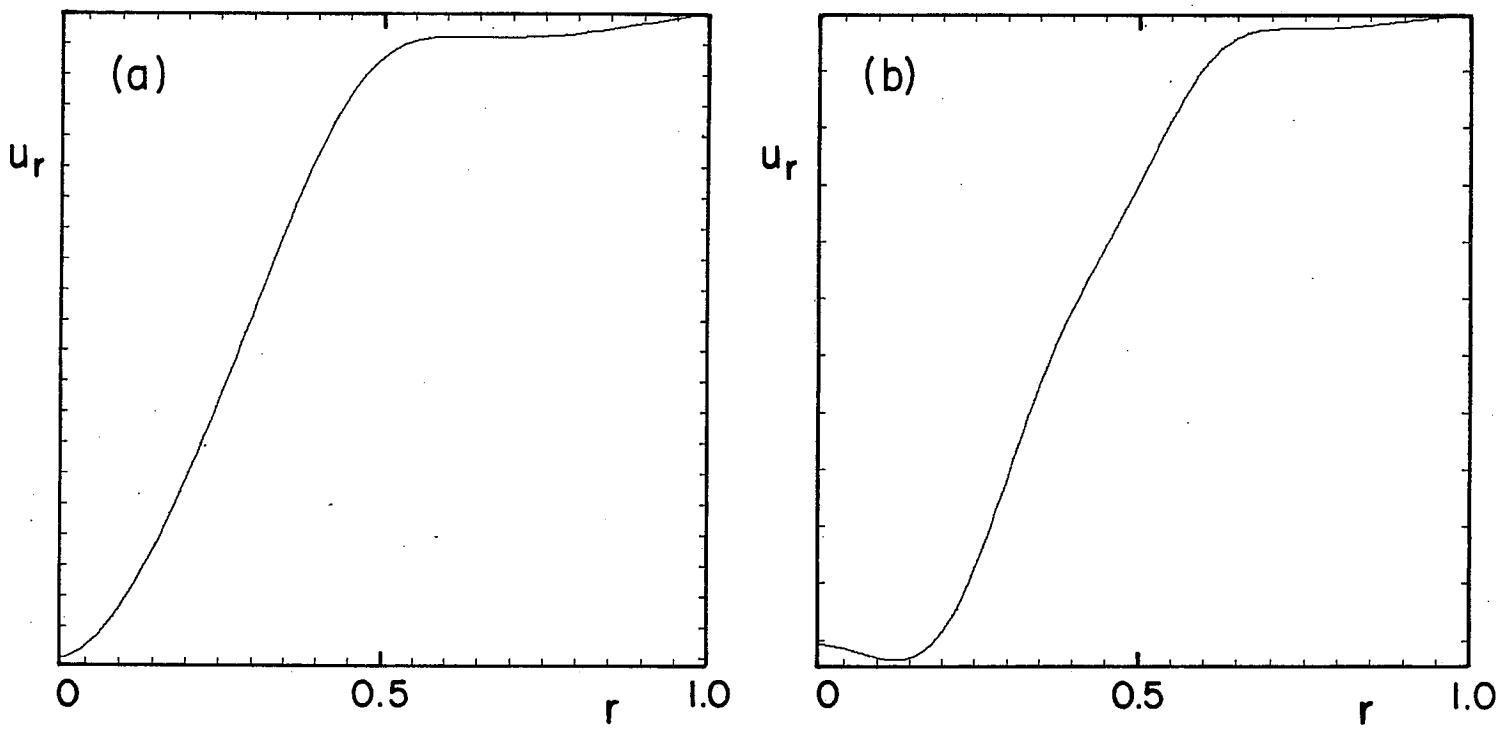

Fig. 3

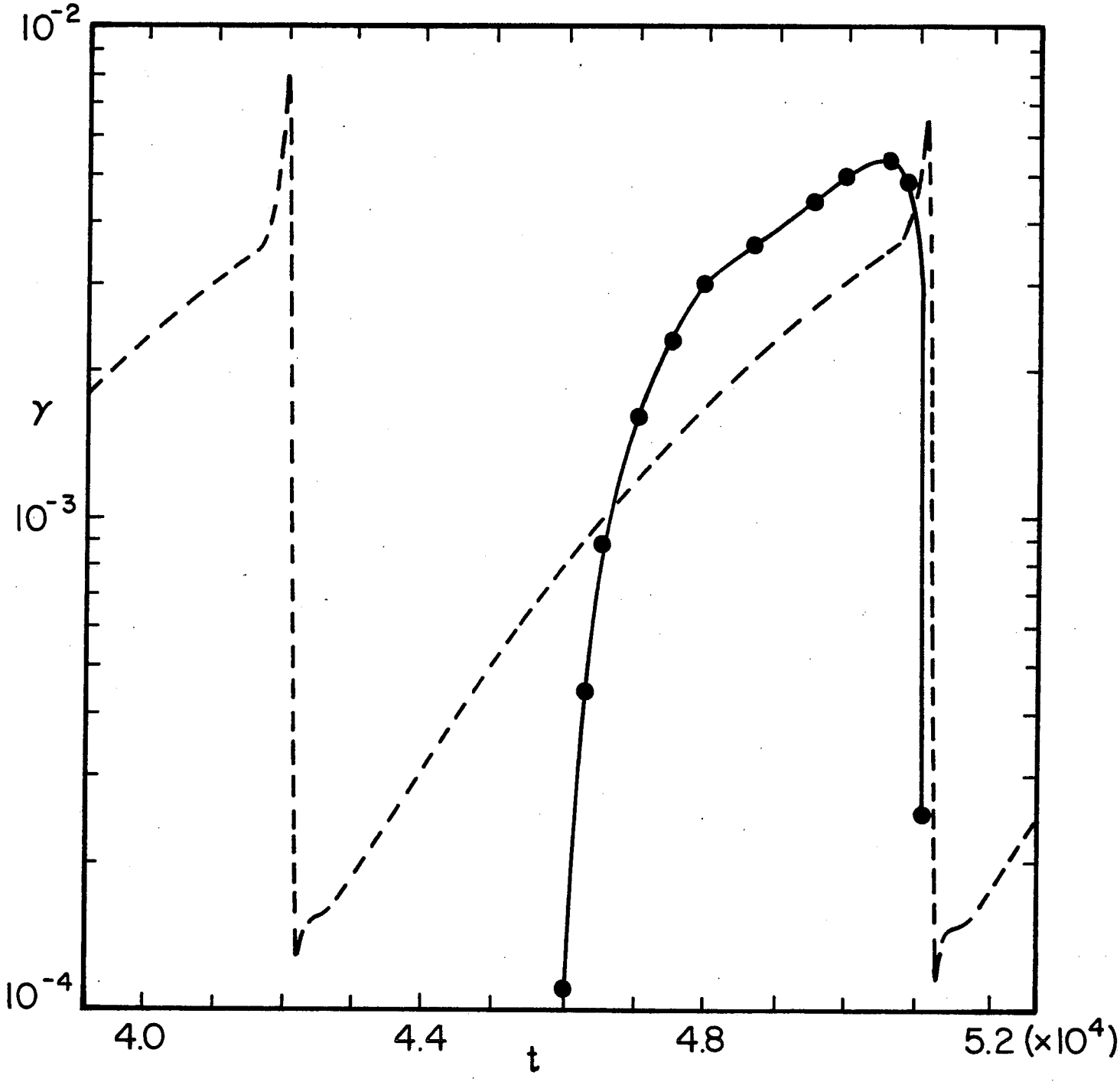

Fig. 4

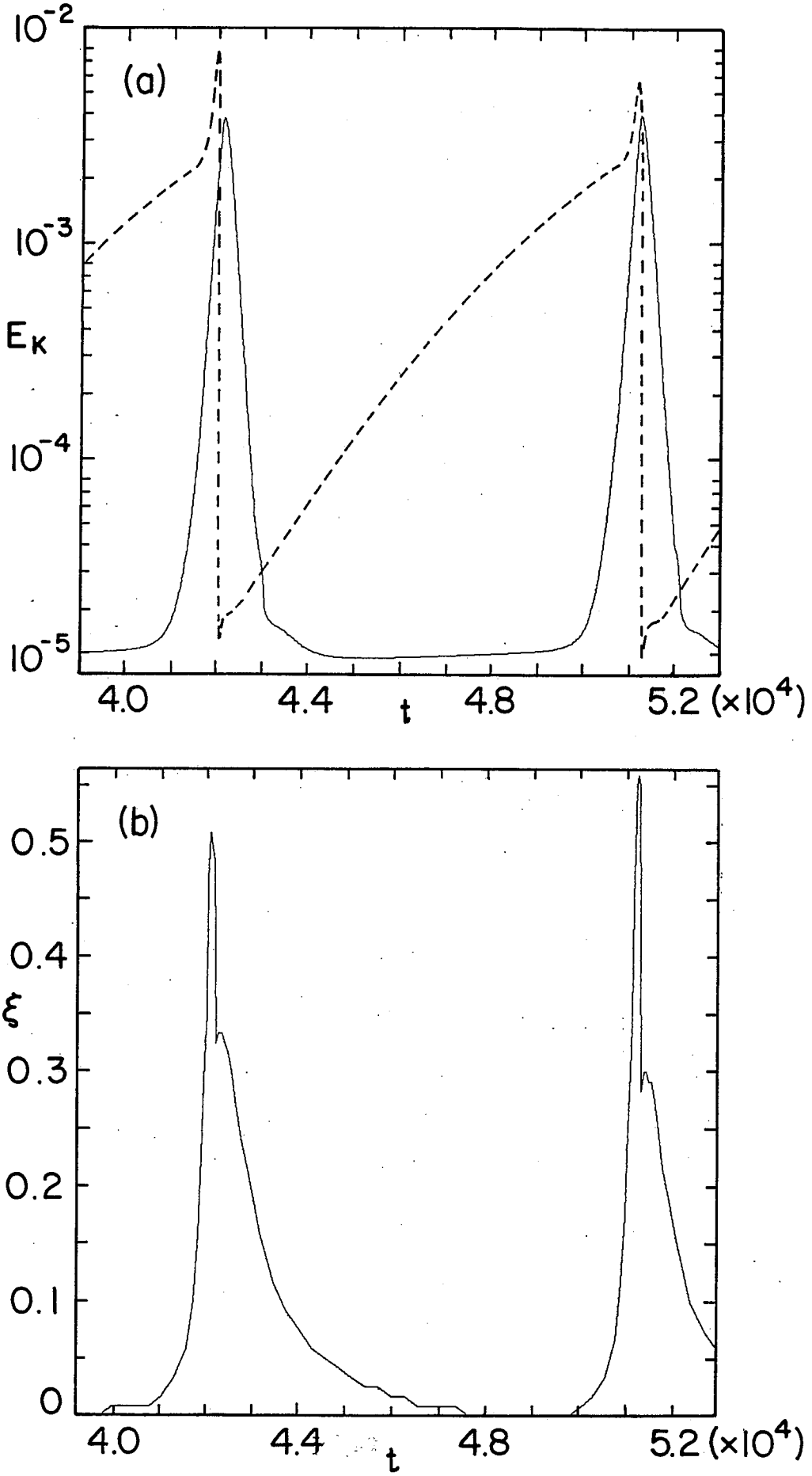
(a)
10^{-2}
10^{-3}
10^{-4}
10^{-5}
E_K
4.0
4.4
4.8
5.2 (×10⁴)
t
(b)
0.5
0.4
0.3
0.2
0.1
0
ξ
4.0
4.4
4.8
5.2 (×10⁴)
t

Fig. 5

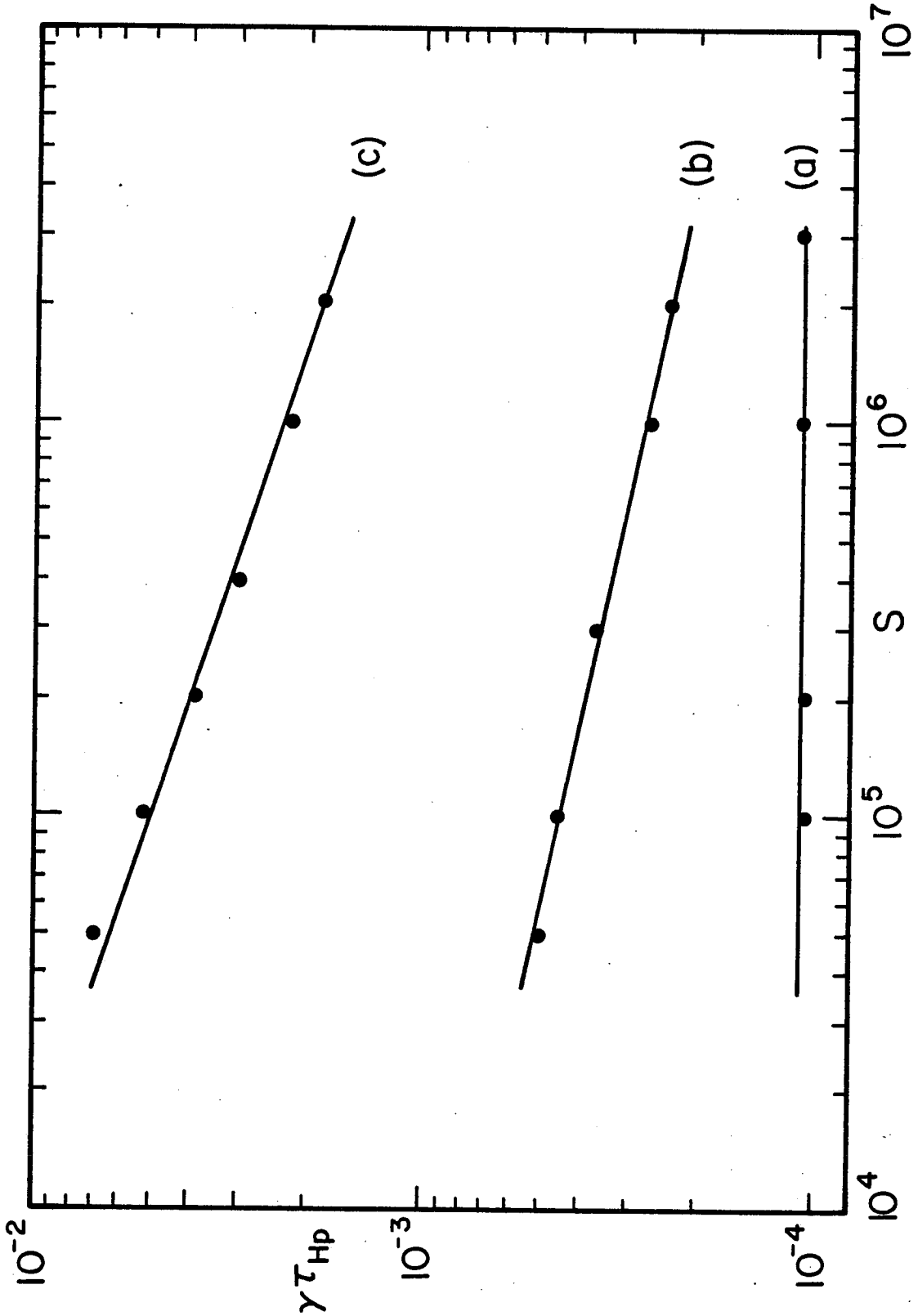

Fig. 6

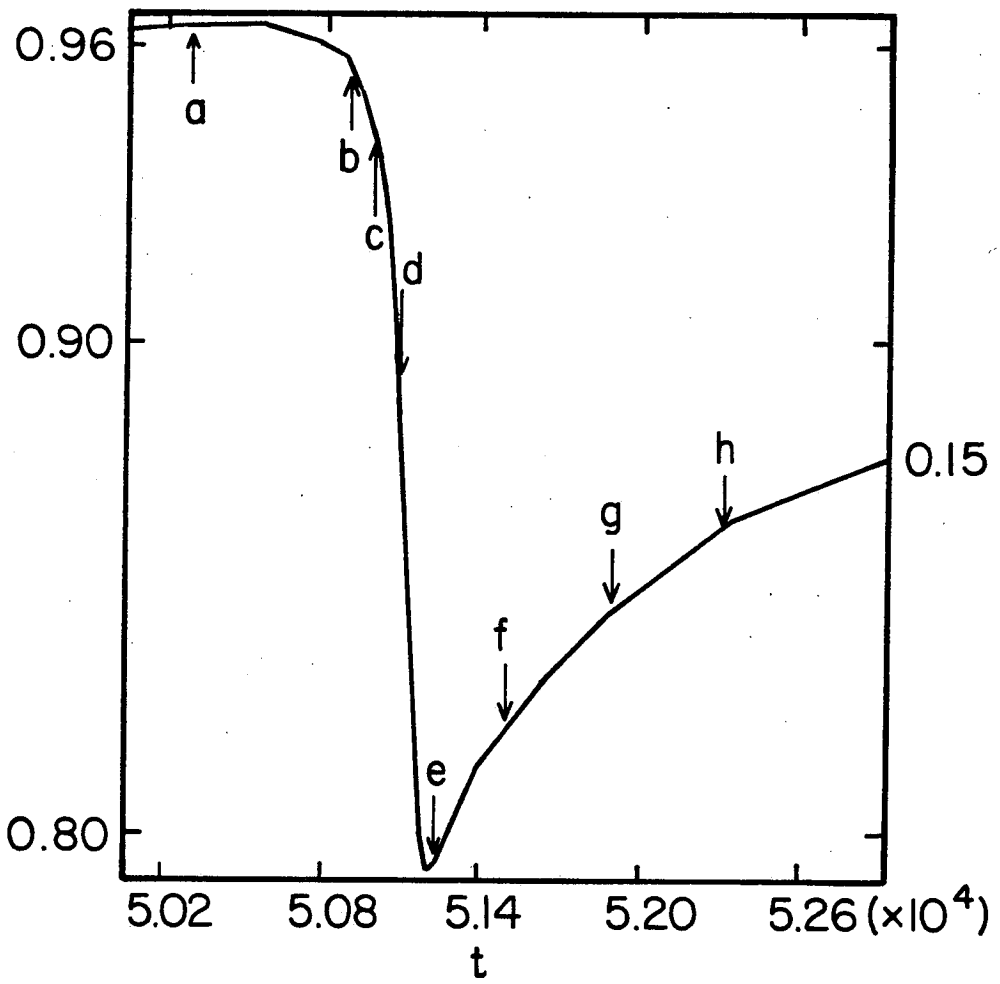

Fig. 7

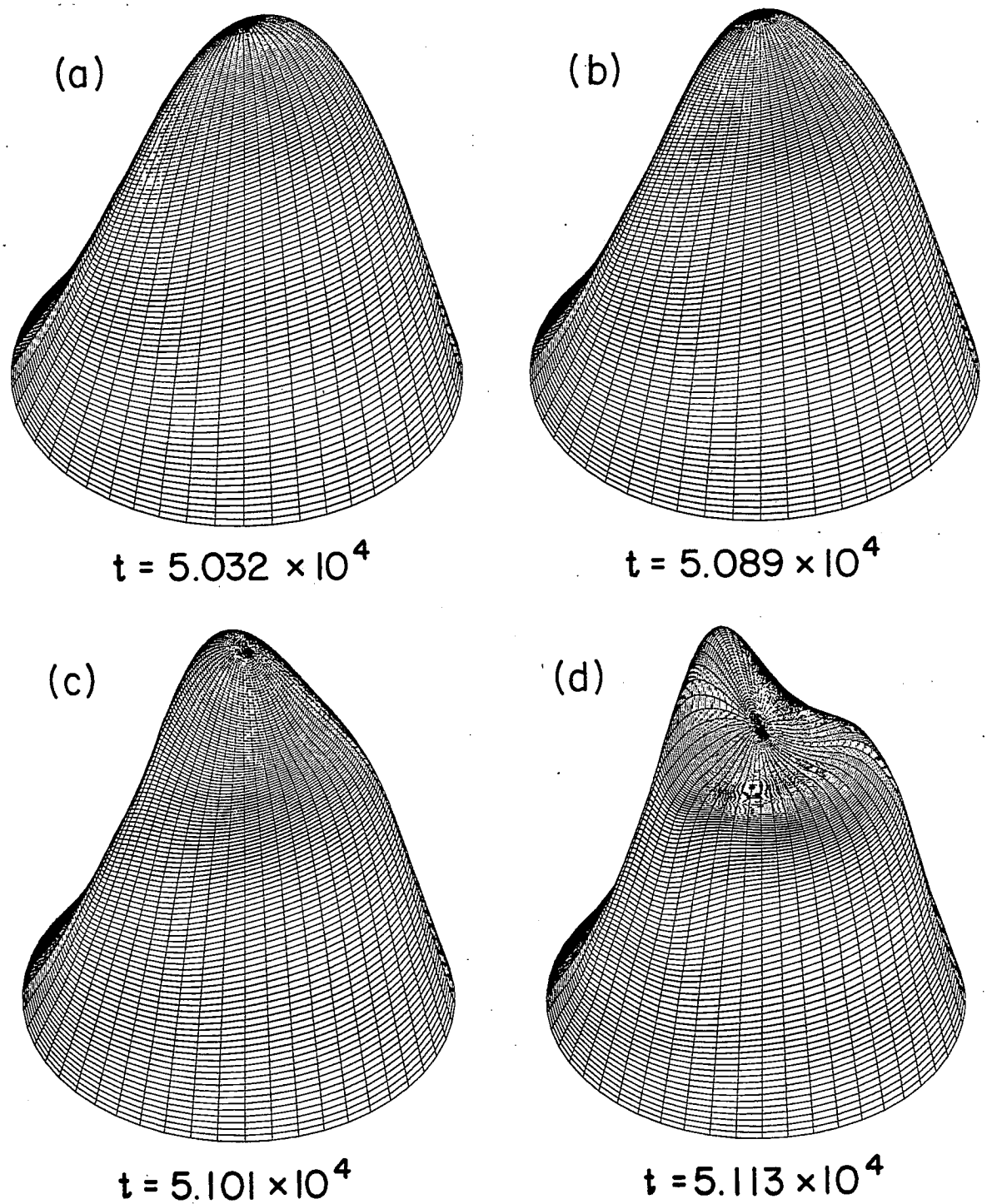

Fig. 8(a-d)

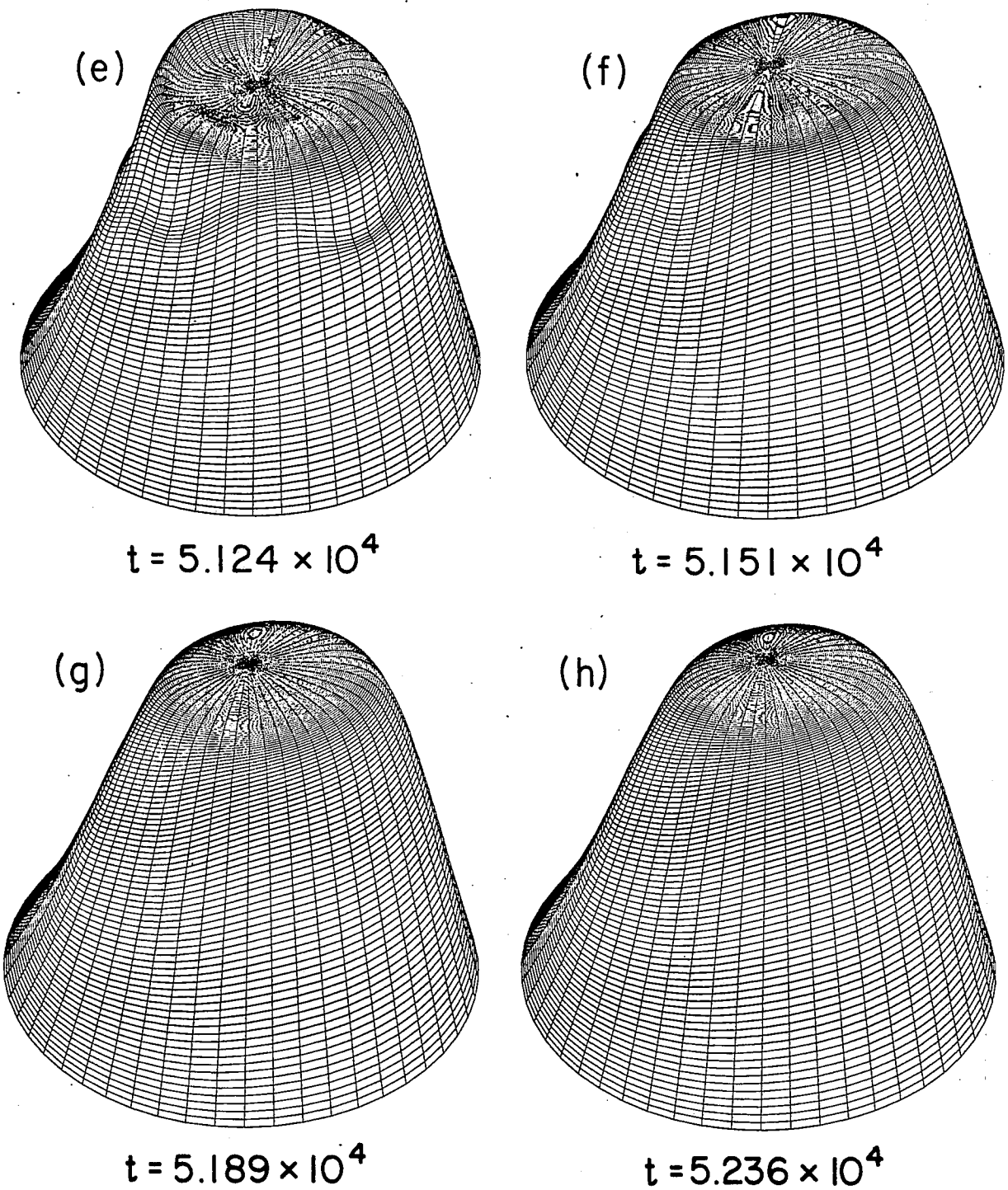

Fig. 8(e-h)

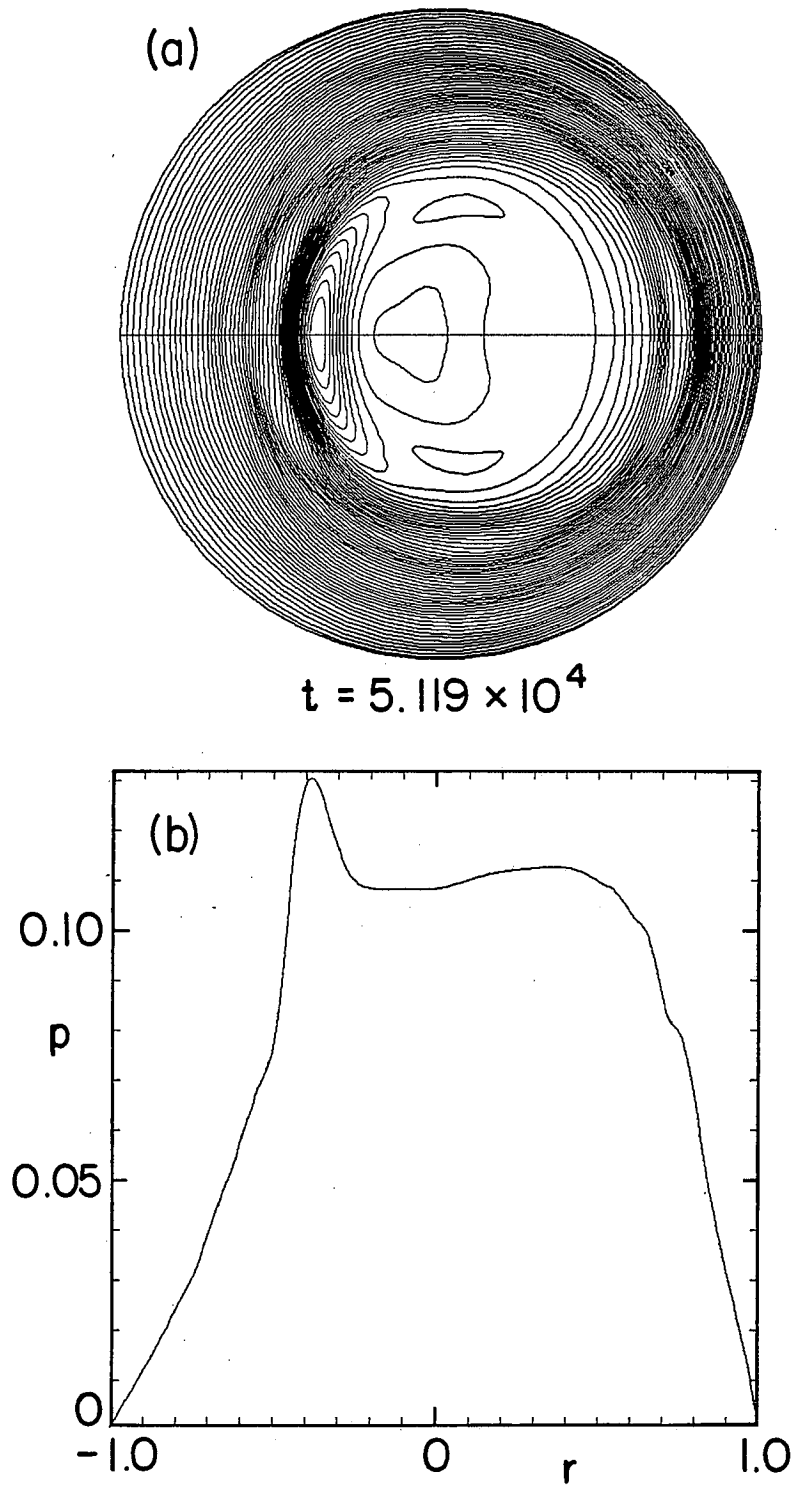

Fig. 9

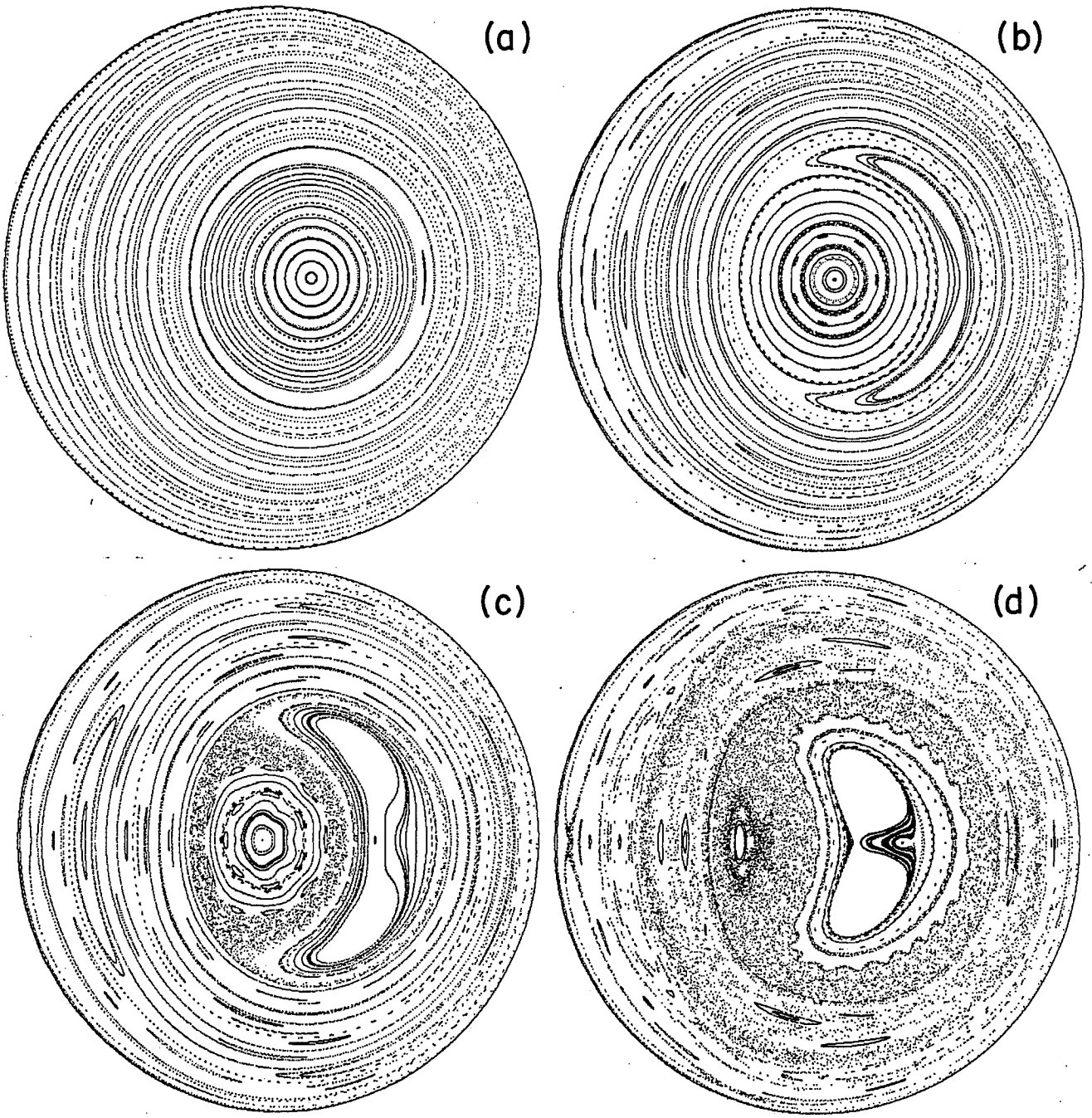

Fig. 10(a-d)

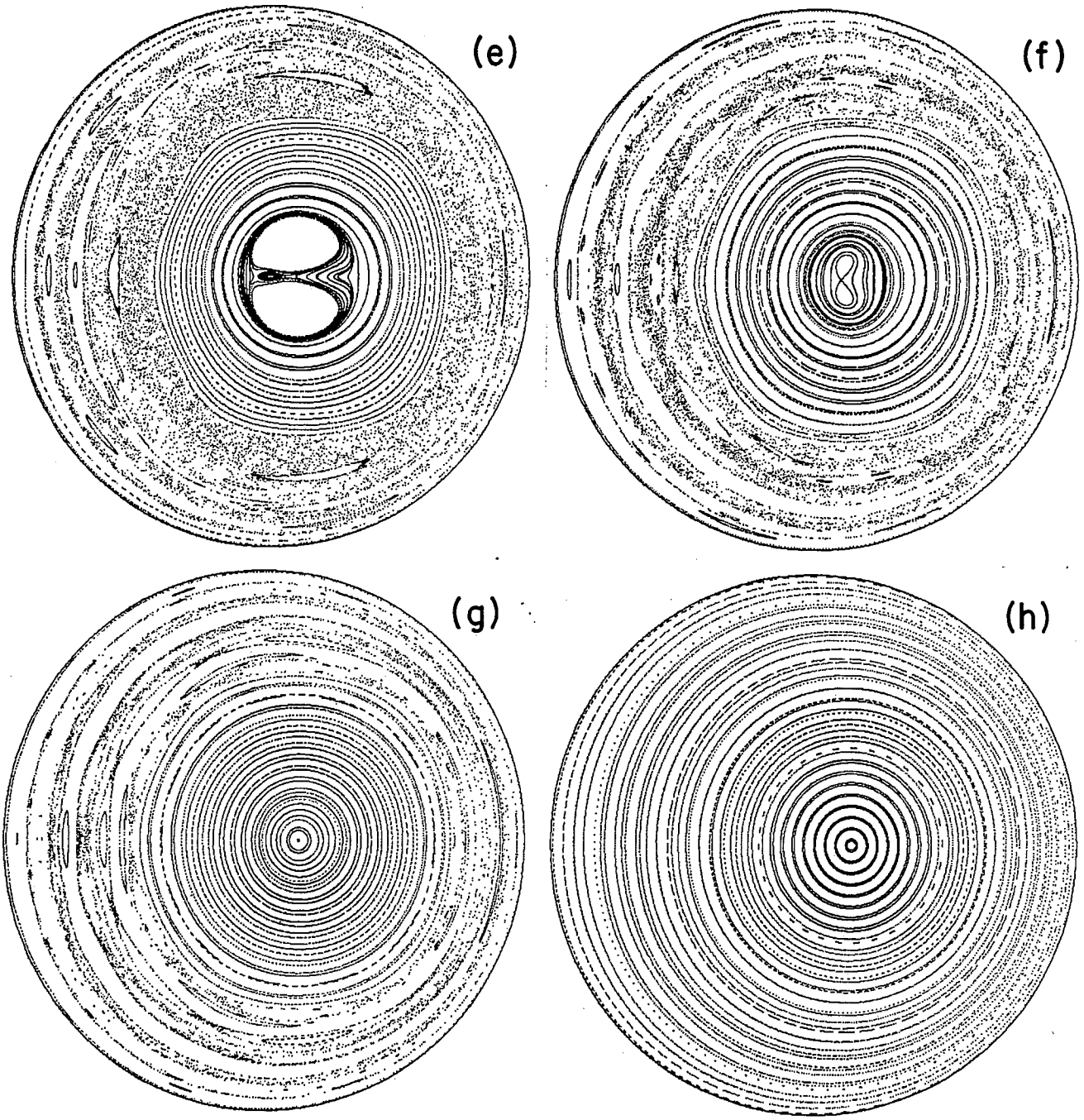

Fig. 10(e-h)

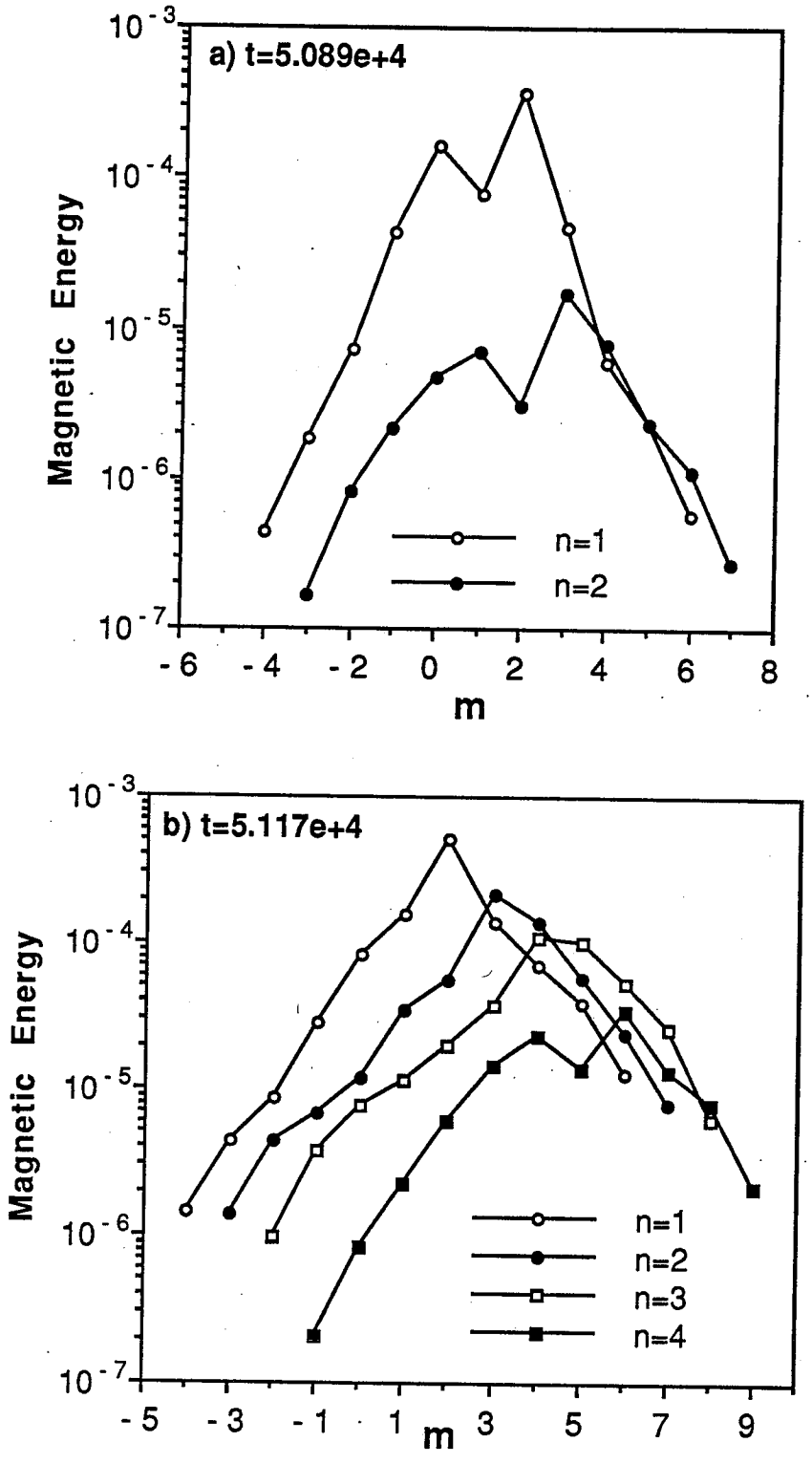
a) t=5.089e+4
Magnetic Energy
m
n=1
n=2
b) t=5.117e+4
Magnetic Energy
m
n=1
n=2
n=3
n=4

Fig. 11

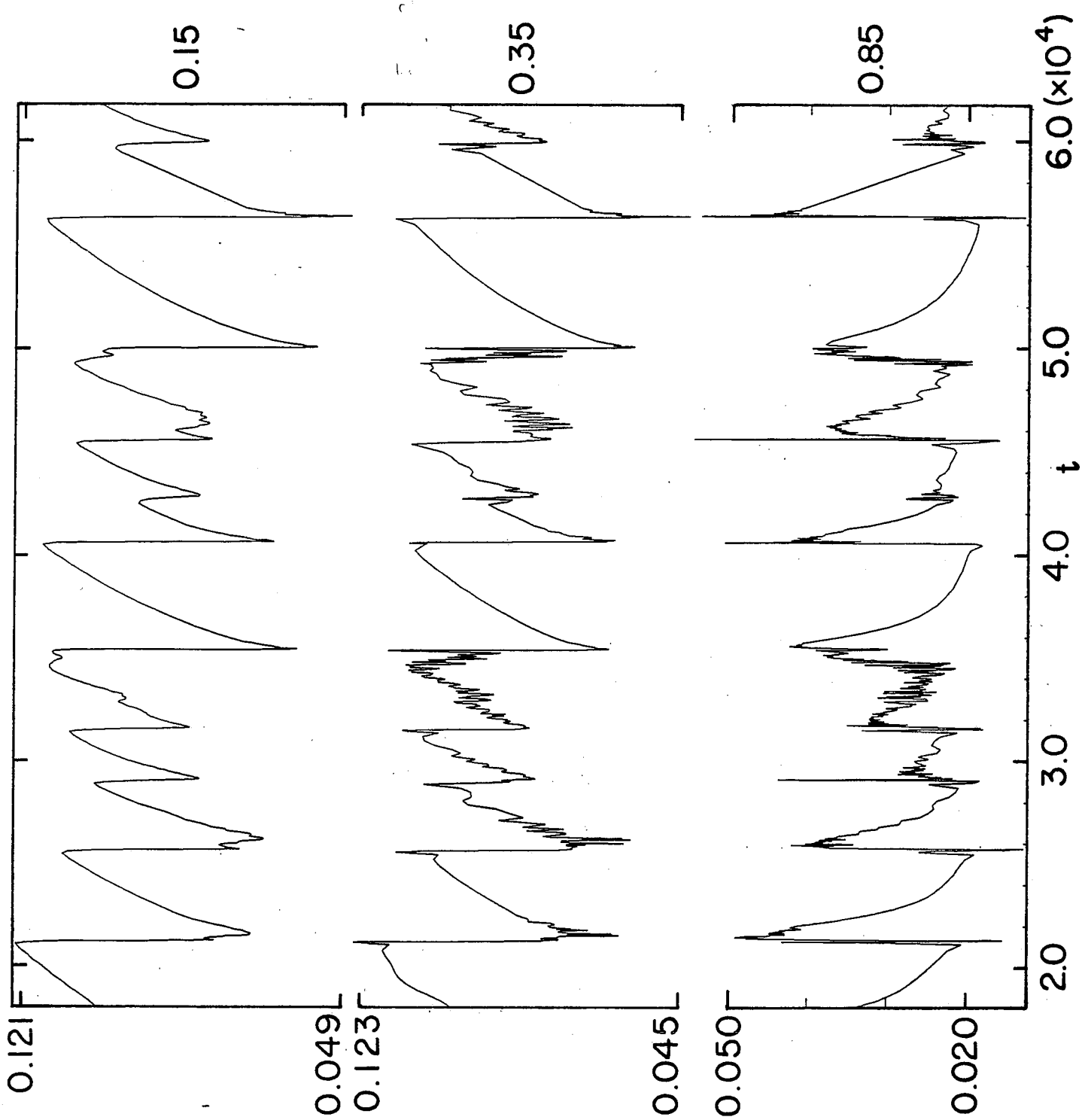

Fig. 12

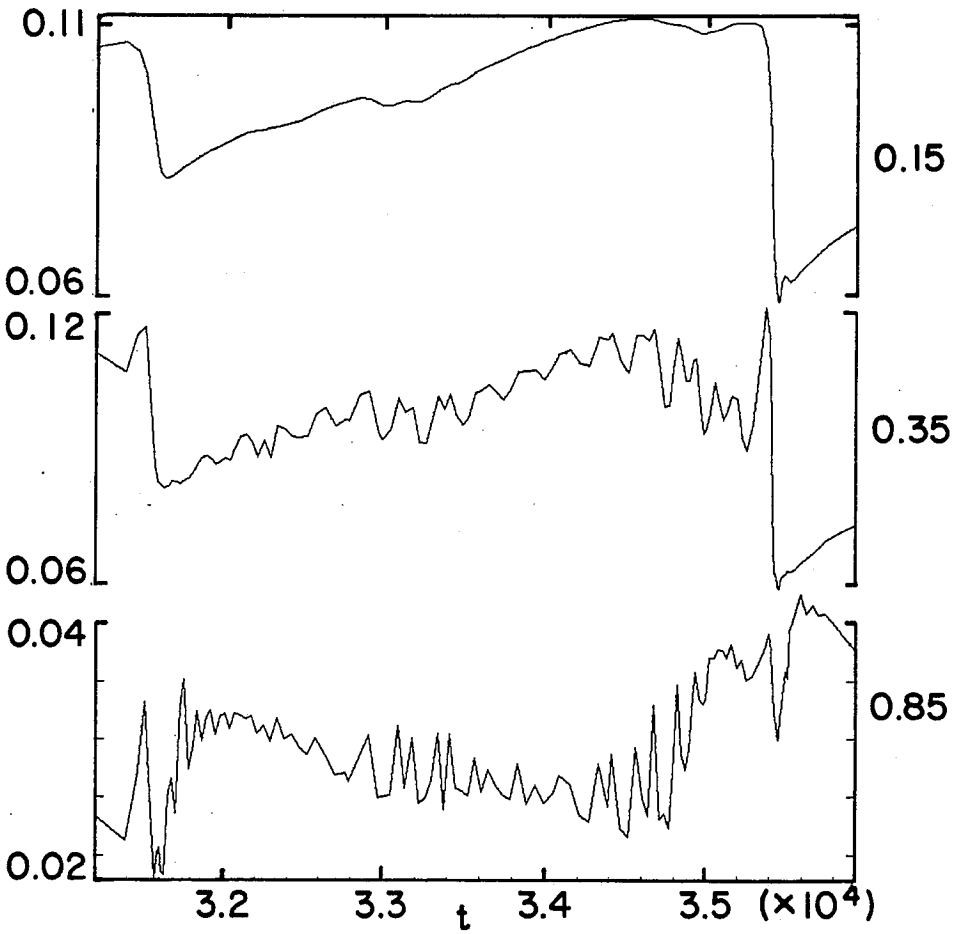

Fig. 13

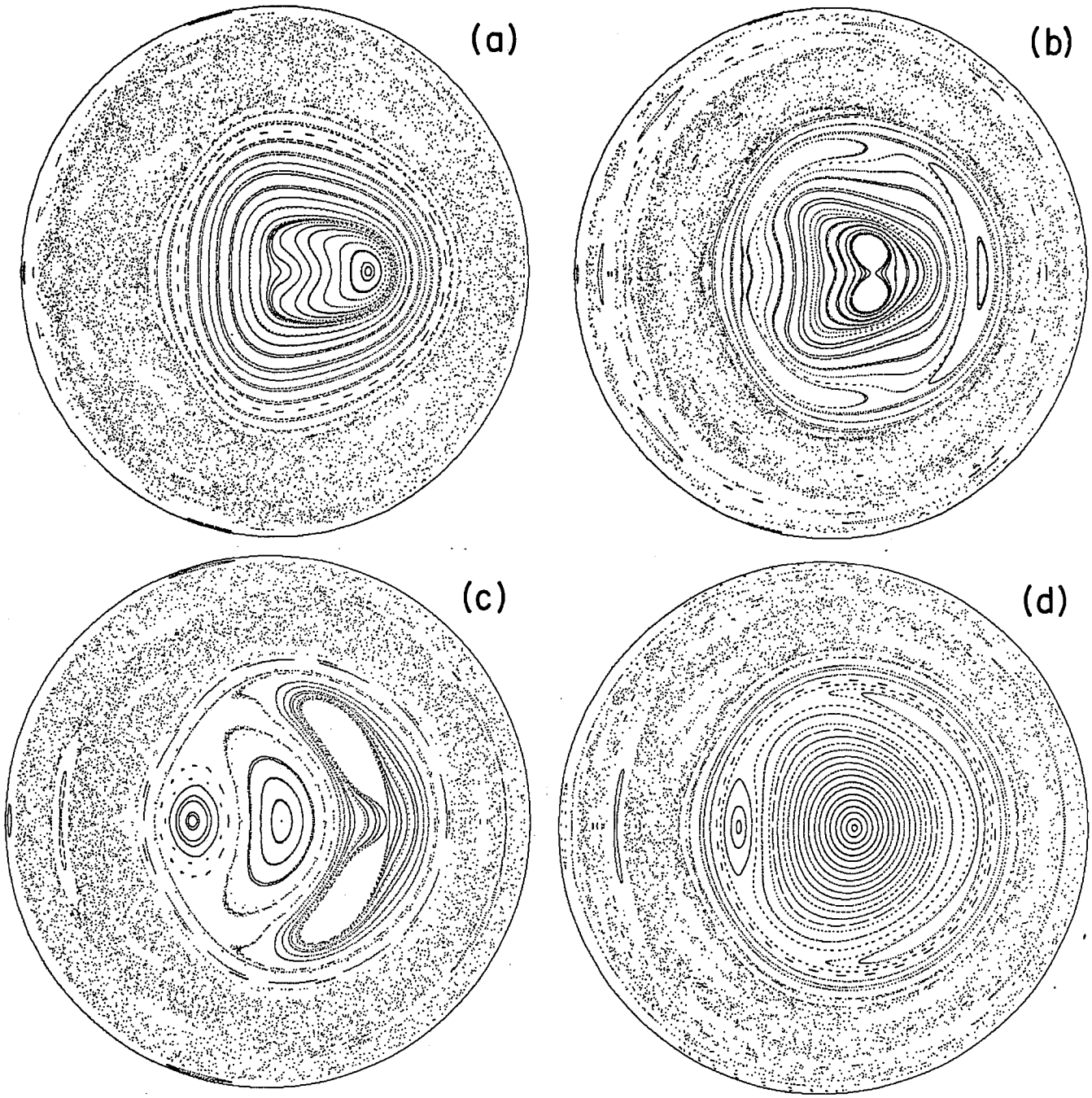

Fig. 14(a-d)

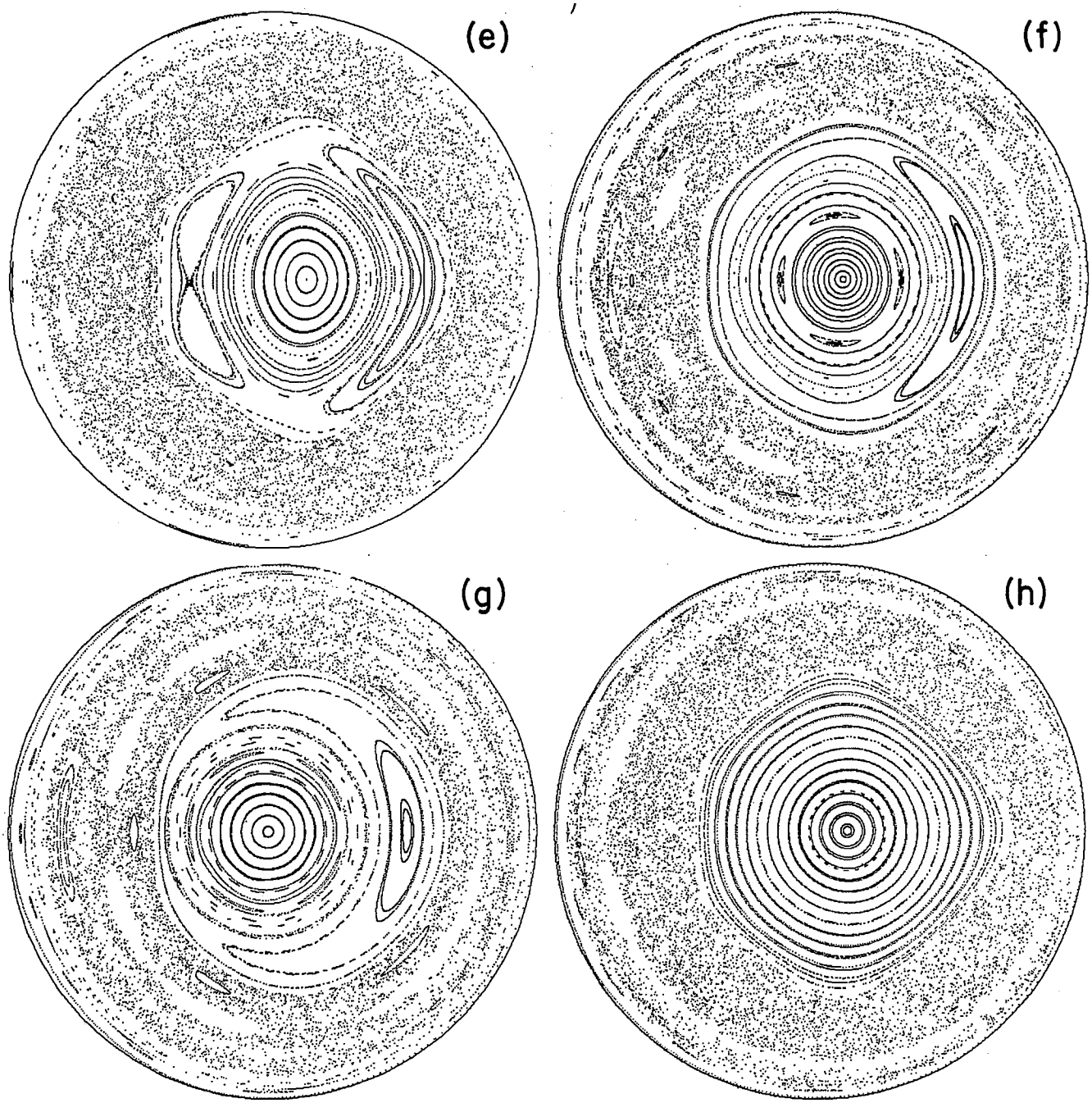

Fig. 14(e-h)

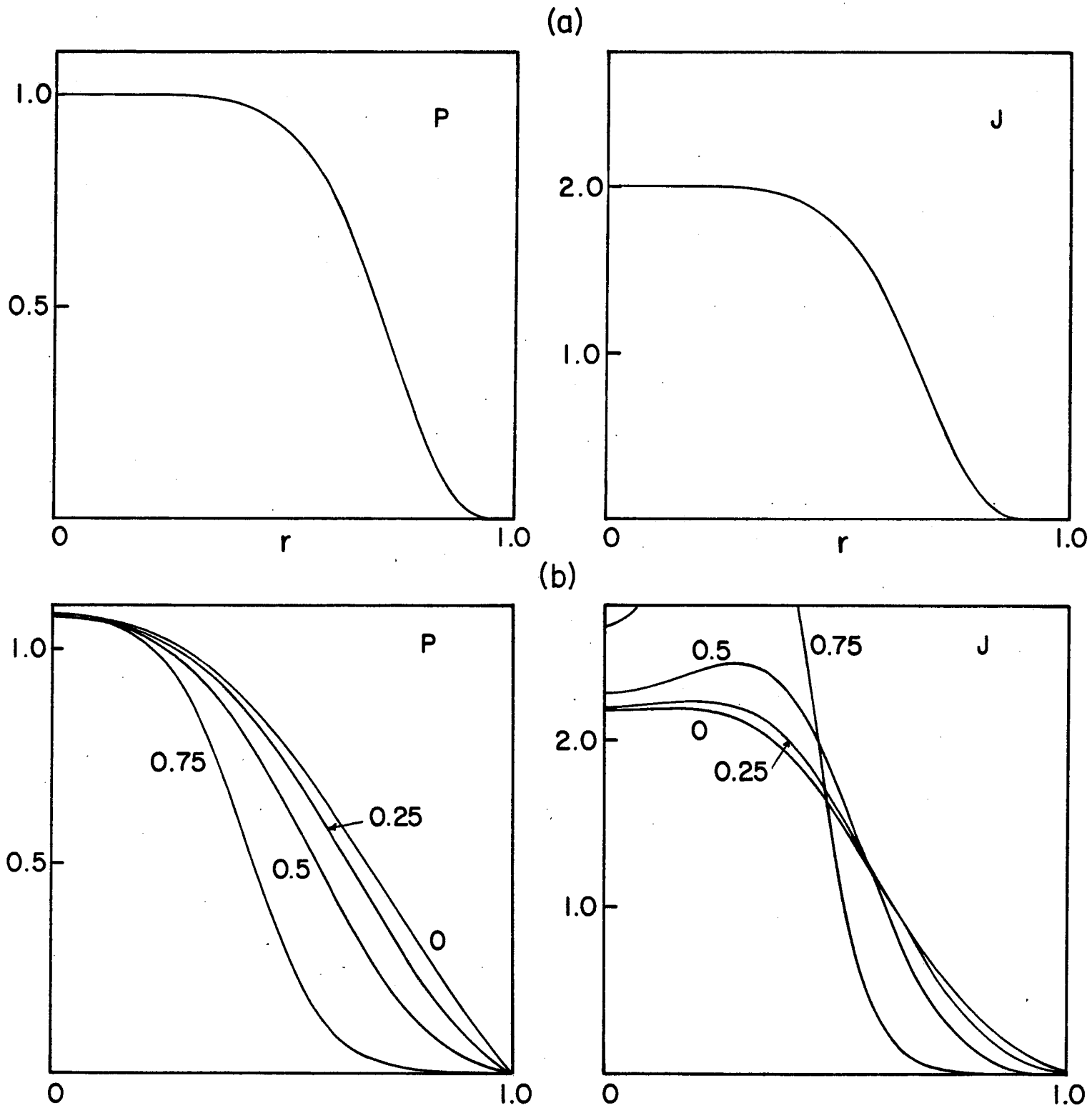
(a)
1.0
0.5
P
0
r
1.0
J
2.0
1.0
0
r
1.0
(b)
1.0
0.5
P
0.75
0.25
0.5
0
0
1.0
J
0.5
0.75
0
0.25
2.0
1.0
0
1.0

Fig. 15

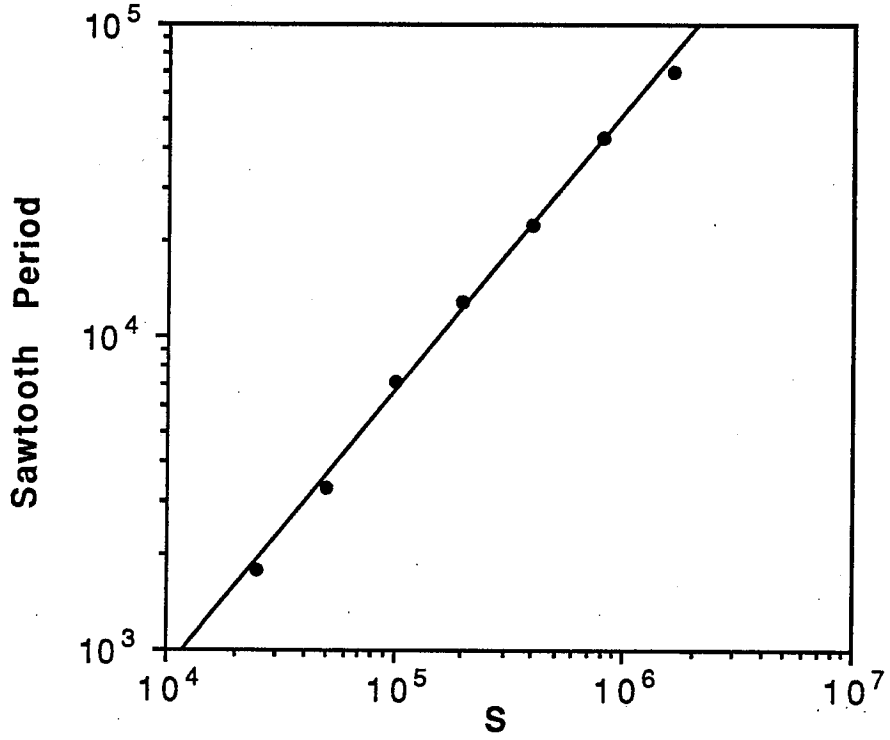

Fig. 16

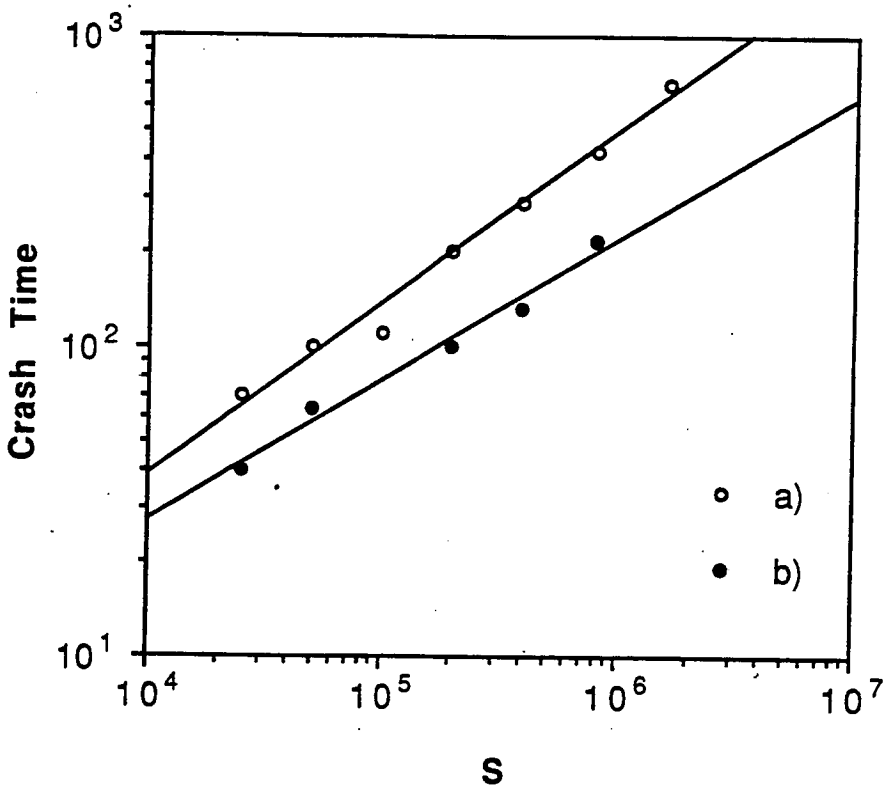

Fig. 17

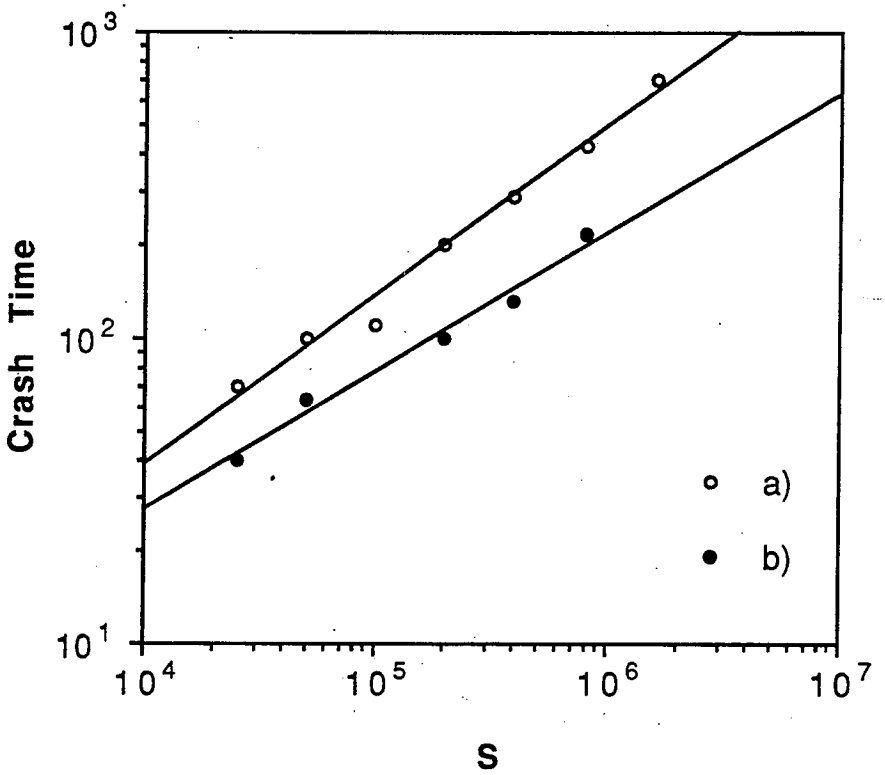

Fig. 17